



# Experimental load modification on a dual-slot circulation control airfoil

Salvatore Asaro<sup>1,2</sup> · Léon Lüer<sup>1,2</sup> · André Bauknecht<sup>1,2</sup>

Received: 9 August 2022 / Revised: 14 October 2022 / Accepted: 11 December 2022 / Published online: 21 December 2022  
© The Author(s) 2022

## Abstract

Active load alleviation can substantially contribute to decrease structural weight and emissions of future transport aircraft by limiting peak aerodynamic loads that the aircraft experiences during flight. Fluidic actuators, as part of active load alleviation systems, have the potential for faster and more complete gust load reduction. The performance of a dual slot circulation control airfoil for gust load alleviation is investigated experimentally on a supercritical airfoil model. The tests are conducted in a low-speed wind tunnel at a chord-based Reynolds number of  $Re = 1.5 \cdot 10^6$  and  $M_\infty = 0.14$ . The model features an elliptical Coandă geometry integrated into the airfoil's trailing edge to minimize cruise performance penalty, while still allowing for substantial load reduction. Blowing from a single slot, as well as simultaneously from pressure and suction side slots is tested over a range of blowing rates to assess the impact on load modification. Both steady and impulsive activation performance are evaluated based on surface pressure, integral load, and flow field measurements around the Coandă geometry. High control authority is found for upper and lower single slot blowing, with peak changes in lift coefficient of about  $\pm 0.33$  and lift-to-equivalent-drag ratio change of up to 100. Similar peak lift changes and reduced equivalent drag are obtained by adding marginal ( $< 14\%$  of total) blowing from the opposite slot, which also reduces pitching moment changes for primary upper and marginal lower blowing. Impulsive jet activation exhibits load control authority comparable to steady actuation and sufficiently short onset times to counteract all gusts defined by certification documentation.

## 1 Introduction

Significant reductions in greenhouse gas emissions are required for future air transport systems to meet increasingly strict environmental regulations. The Flightpath 2050 report issued by the Advisory Council for Aeronautics Research in Europe (ACARE) defines target reduction rates of 75% for  $CO_2$  and 90% for  $NO_x$  compared to a conventional aircraft from 2000 (Darecki et al. 2011). To reach these ambitious goals, new technologies have to be identified that can reduce structural weight, aerodynamic drag, fuel consumption, and corresponding emissions. The structural weight of the wings

is mainly governed by the requirement to withstand large dynamic loads induced by maneuvers or the interaction with an upwards directed gust. Consequently, the wing is sturdier and correspondingly heavier than it could be without these dynamic loads. One way to reduce the structural requirements is the reduction of dynamic loads through use of active load alleviation. Several studies have investigated the potential of active methods for gust load alleviation (GLA), with a focus on utilizing the available conventional control surfaces on the airplane such as spoilers (Mickleboro 1948) and ailerons (Regan and Jutte 2012).

The certification specifications CS-25 of the European Aviation Safety Agency (EASA) (EASA 2020) define a range of deterministic vertical gusts of 1-cos shape with different lengths that the aircraft have to be able to withstand over the entire flight envelope. An active GLA system based on conventional sensors for gust detection and existing control surfaces for actuation is not capable of counteracting the dynamic loads caused by all relevant gust lengths due to the limited slew rates. The required faster actuation speeds to compensate all 1-cos gusts (Geisbauer and Löser 2017) are difficult to reach due to the control surface inertia and onset

✉ Salvatore Asaro  
s.asaro@tu-braunschweig.de

<sup>1</sup> Institute of Fluid Mechanics, Technische Universität Braunschweig, Hermann-Blenk-Str. 37, 38108 Brunswick, Lower Saxony, Germany

<sup>2</sup> Cluster of Excellence SE2A (Sustainable and Energy-Efficient Aviation), Technische Universität Braunschweig, Hermann-Blenk-Str. 37, 38108 Brunswick, Lower Saxony, Germany

of fatigue problems at highly dynamic actuation (Hönlinger et al. 1994). Even considering that the shorter 1-cos gusts may not be responsible for the peak structural loads (Xu 2012), any gains in actuation speed will greatly benefit overall performance of a full GLA system, which experiences time delays due to the employed gust sensing and controller.

Research in the past years has been focused on dedicated GLA and maneuver load alleviation (MLA) systems that work independently or in support of the primary aircraft controls (Blaylock et al. 2014; Chambers 2005; Li and Qin 2020), with the goal to realize faster actuation times and spanwise-optimal load reduction. These actuation systems can be categorized as either mechanical—like ailerons, spoilers, micro-tabs, or bumps—or as fluidic—like air jets blown normal to the airfoil's surface or tangentially over a rounded trailing edge. Two-dimensional Reynolds-Averaged Navier–Stokes (2D-RANS) simulations show that several of these actuation designs have the potential to compensate the gust-induced peak lift change, but only the conventional aileron, a jet normal to the airfoil's surface (normal jet), and a tangential jet over a rounded trailing edge (Coandă jet) combine high peak lift reductions with small changes in drag and pitching moment over the entire flight envelope (Khalil et al. 2021).

The main advantages of the normal jet and Coandă jet over the conventional aileron are their reduced mechanical complexity and potential for highly increased actuation rates, enabling them to quickly react even to the fast load changes induced by the shortest 1-cos gusts encountered in flight. As other fluidic actuators, the normal and Coandă jet are typically powered by bleed air extracted from the jet engine low-pressure compressor. This extracted mass flow slightly reduces jet engine performance and therefore manifests as an additional drag component in the overall aircraft power balance (Radespiel et al. 2016). This power requirement of a fluidic actuator is classically expressed as the momentum coefficient  $c_\mu$ :

$$c_\mu = \frac{\dot{m}_{\text{jet}} \cdot v_{\text{jet}}}{\frac{1}{2} \rho_\infty U_\infty^2 S_{\text{ref}}} \quad (1)$$

where  $\dot{m}_{\text{jet}}$  is the required jet mass flow rate,  $v_{\text{jet}}$  the jet velocity,  $\rho_\infty$  the ambient air density,  $U_\infty$  the freestream velocity, and a reference area  $S_{\text{ref}} = c \cdot b$ , i.e. chord times span. The values of  $c_\mu$  are reported as percentages throughout this paper for better readability.

The altered trailing edge shape to implement the Coandă actuator has a detrimental effect on baseline airfoil performance, mainly on the drag coefficient. It has been shown that the baseline performance can be recovered using continuous blowing with very low values of  $c_\mu$  from slots on both the upper and lower airfoil side (Jones 2005). However, the Coandă jet is highly efficient in creating lift changes during

GLA operation, resulting in  $c_\mu$  requirements that are between two and nine times smaller than for the normal jet (Asaro et al. 2021). For this reason, the focus of the present study is on the Coandă actuator as the most promising candidate for active GLA.

The high efficiency of the Coandă actuator in terms of lift change is due to it leveraging the so-called Coandă effect. Its application for circulation control on airfoils has been studied for the past 70 years. This effect describes the tendency of a jet to attach itself to an adjacent wall due to a difference in static pressure with respect to the outer flow, enabling it to follow even highly convex surface contours. These convex surfaces can be implemented in the trailing edge region of an airfoil with upstream slots on both upper and lower side that produce tangential jets over these Coandă surfaces. Mixing between wall-bound jet and outer flow causes entrainment of the outer flow and momentum exchange that stabilizes the boundary layer. This enables high levels of flow turning around the convex Coandă surfaces, leading to a shift of the trailing edge stagnation point and corresponding control of airfoil circulation and lift. Activation of the upper jet leads to increased airfoil lift, whereas the lower jet reduces lift.

Based on available literature, a linear lift change is expected with increasing  $c_\mu$  for small values of  $c_\mu$ , in the so-called boundary layer control region (Englar and Williams 1971; Abramson 1975; Alexander et al. 2005). For larger blowing rates, in the so-called circulation region, a square root dependency is found that converges asymptotically against a limit that corresponds to the condition where the jet is fully wrapped around the Coandă surface (Miklosovic et al. 2016). For this reason, the Coandă actuator exhibits the best lift gain factor  $\Delta c_L / c_\mu$  in the boundary layer control region, i.e. with relatively small values of  $c_\mu$ , but adequate lift change for GLA.

There are few studies that have analyzed the temporal behavior of a Coandă-type flow actuator integrated in a clean airfoil and intended for GLA or MLA. Unsteady RANS simulations of a symmetrical airfoil showed that adequate activation of a Coandă jet can lead to a near constant lift when the airfoil encounters a medium-amplitude 1-cos gust (Li and Qin 2020). Unsteady 2D-RANS simulations of a supercritical airfoil at different operating conditions indicated that an impulsive activation of a Coandă jet can reach lift reduction amplitudes within a reaction time that is suitable also for compensating the shortest 1-cos gusts (Asaro et al. 2021). The fast onset of actuator-induced lift was further illustrated by an experimental study of a cambered airfoil at low Reynolds number. The low slot blowing showed high control authority and promisingly fast reaction time suited to counteract gust-induced load (Düssler et al. 2022).

The present work deals with the application of a dual-slot circulation control airfoil for GLA and MLA implemented in a supercritical airfoil without high-lift devices.

The goal is to realize an actuator with minimal effects on the airfoil’s baseline performance and sufficiently high lift control authority to alleviate typical gust-induced loads. A subsonic and modular wind tunnel model was designed and tested in a low-speed wind tunnel. The focus of this work is on the steady actuator performance achieved for both single- and dual-slot blowing, as well as the unsteady performance of the actuation system for impulsive switching between upper and lower blowing. The present study is conducted in the framework of the Cluster of Excellence SE<sup>2</sup>A on Sustainable and Energy-Efficient Aviation and its implementation in the overall research program is described in detail in (Bauknecht et al. 2022).

## 2 Experimental setup

### 2.1 Wind tunnel and airfoil model

A wind tunnel test was conducted in the low speed wind tunnel MUB at Technische Universität Braunschweig. The Göttingen-type wind tunnel has a closed test section of 1.3 m × 1.3 m × 6 m with a maximum freestream velocity of 60 m/s and constant temperature controlled through a heat exchanger. The tests were conducted with a custom built 2D airfoil circulation control model, which was mounted vertically in the test section, as shown in Fig. 1. The model has a chord length of  $c = 0.5$  m, span of  $b = 1.3$  m, and was tested at a constant freestream velocity of  $U_\infty \approx 50$  m/s, resulting in a chord-based Reynolds number of  $Re \approx 1.5 \cdot 10^6$  and  $M_\infty \approx 0.14$ .

The wind tunnel model is based on the DLR F15 airfoil without high-lift devices. The implementation of a dual-slot Coandă-type flow actuator in its trailing edge section is illustrated in Fig. 2, with the adapted shape and surface pressure locations in Fig. 2a and a zoomed-in photograph of the trailing edge region without side covers in Fig. 2b. In order to integrate the flow actuator into the trailing edge region, the thickness of the airfoil was sinusoidally increased aft of the 0.53c position. Correspondingly, the trailing edge thickness is increased by a factor of eight compared to the original geometry, which allows the integration of an elliptical Coandă surface.

The characteristic design parameters of a Coandă actuator are the shape of the convex surface, its radius  $r$ , jet slot height  $h$ , and lip height  $l$ . Higher values of  $r$  cause less severe flow turning and consequently longer attachment of the jet on the surface and higher lift change, but also lead

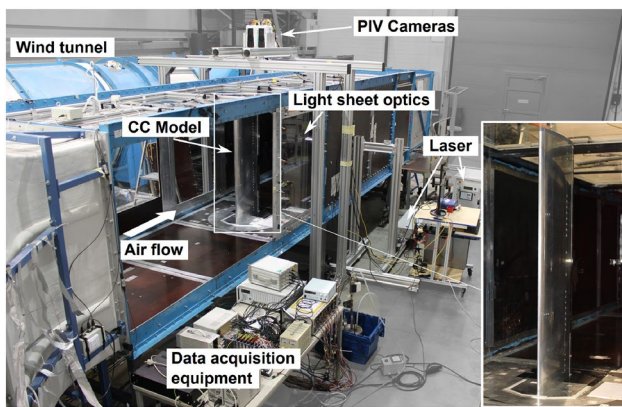
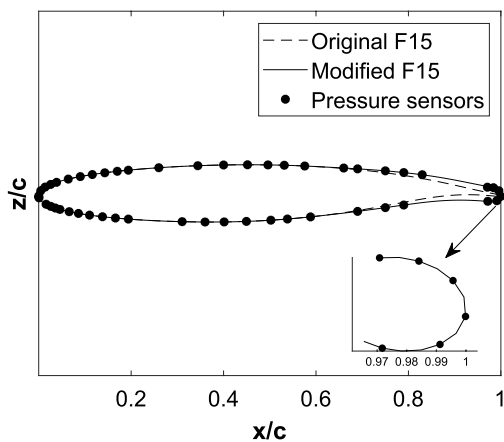
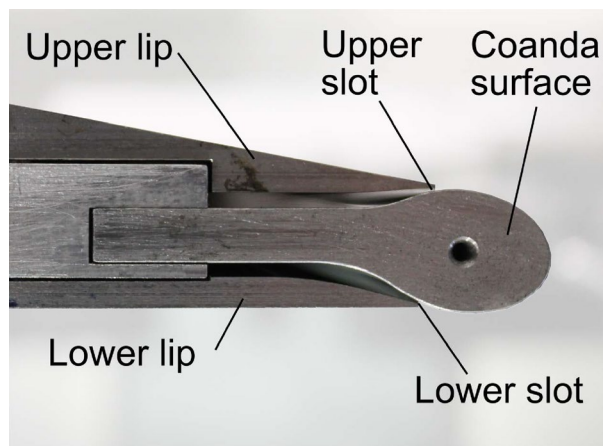


Fig. 1 Experimental setup of dual-slot Coandă model in MUB wind tunnel



(a) Sketch of airfoil contour



(b) Coandă geometry with lips, slots, and curved Coandă surface

Fig. 2 Original and modified airfoil contour and detail view of actuator geometry

to increased drag penalties when the actuator is not in use. The selected elliptical shape increases the effective radius of the Coandă surface for a given height of the airfoil's trailing edge section. This has been shown to create smaller drag penalties on the unblown airfoil than a circular shape, but slightly reduced performance for high lift applications, which are not targeted here (Jones 2005). Elliptical surfaces are also more suitable for applications under transonic flow conditions (Alexander et al. 2005), for which the airfoil was originally designed, leading to slightly reduced performance in the currently tested subsonic flow regime. An elliptical shape has been selected here as a compromise between required lift change for gust load alleviation and to minimize performance loss of the unblown airfoil.

A general principle of the circulation control airfoil is that for a given value of  $c_{\mu}$  smaller slot heights  $h$  lead to increased jet velocity  $v_{\text{jet}}$ , reduced mass flow requirements  $\dot{m}_{\text{jet}}$ , and—at least in the sub-critical regime with jet Mach numbers below 1—to increased lift changes (Abramson 1975). A small slot height was therefore targeted in the current design. Previous experimental research has identified combinations of slot height  $h$  and surface radius  $r$  that lead to favorable Coandă performance, e.g. with  $2\% < r/c < 5\%$  and  $h < 0.25\%c$  (Englar and Williams 1971). However, more recent results have shown that these values do not constitute hard limits, as even smaller slot heights  $h < 0.05\%c$

and radii  $r/c < 0.5\%c$  have been shown to result in good actuator performance (Warsop and Crowther 2018). The current design incorporates an effective Coandă radius in the optimal design range defined by Englar and Williams (1971). The ellipse has a minor axis of  $3.1\%c$  and major axis of  $4.6\%c$ , which is aligned with the local airfoil camber and forms a downward angle of  $8.5^\circ$  with the chord line, as listed in Table 1.

Finally, the ratio of lip height  $l$  to slot height  $h$  also impacts actuator performance, because the wake region behind the lip influences the interaction between Coandă jet and outer flow. Increased values of  $l/h$  above unity lead to reduced downstream velocity of the jet and consequently earlier jet detachment from the surface and smaller lift change (Nishino and Shariff 2012). The lip-to-slot ratio was therefore kept at unity in the present design.

The design height of both the upper and lower slot of the Coandă actuator is  $h = 0.08\%c$  or 0.4 mm. The lips between the actuator slots and outer flow have the same minimal thickness at the slot position of  $l = 0.08\%c$ , but rapidly increase in thickness forward of the slots for increased rigidity, as shown in Fig. 2b. The majority of the model is milled out of aluminum, whereas the lips and Coandă surface are made from steel to minimize deformations, and part of the internal pressurized air system is created using rapid prototyping.

The inside of the model is hollowed out to contain the multiple components of the circulation control system, the layout of which is shown in Fig. 3. An 8 bar air compressor supplies the pressurized air to the actuation system through the model root. The air flow is controlled by three proportional valves connected to three mass flow meters—two for the lower slot jet and one for the upper jet. This setup allows for exact control of the average mass flow rates  $\dot{m}$  and consequently  $c_{\mu}$ . In addition, a total of nine fast acting multi-level valves are used for fast adjustment

**Table 1** Circulation control airfoil characteristics

Trailing edge shape		Ellipse
Minor axis		$3.1\%c$
Major axis		$4.6\%c$
Slot heights	$h$	$0.08\%c$
Lip heights	$l$	$0.08\%c$
Major axis angle		$8.5^\circ$

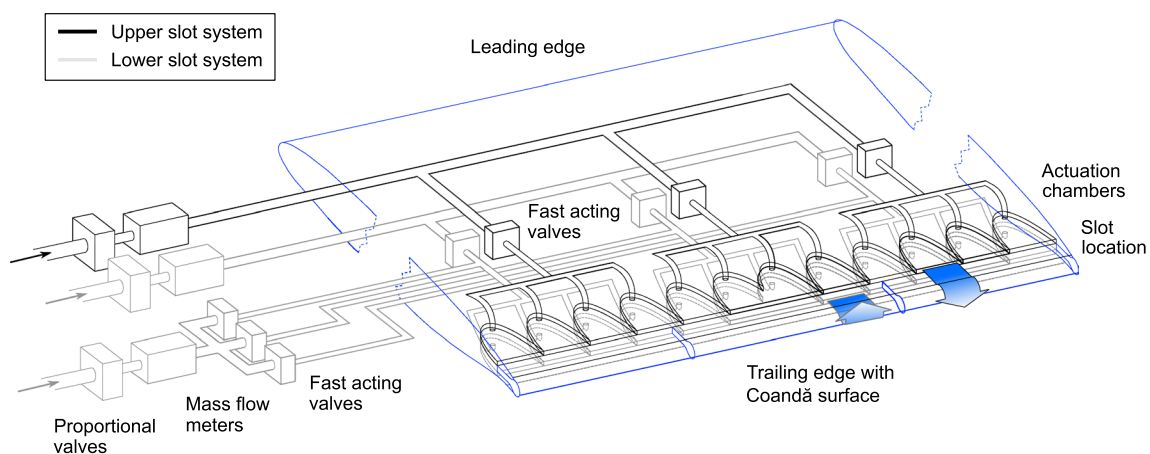


**Fig. 3** Schematic of the pressurize air system for the upper and lower jet

of jet flow rates at multiple discrete levels. Six of these fast acting valves are integrated inside the model and three outside, whereby the lower slot is fed by combined mass flow from three internal and three external valves. The model contains a total of 24 3D-printed actuation chambers (12 for the lower and 12 for the upper slot) that are shaped similar to the inside of a Rankine half-body. These shapes have been shown to produce spanwise homogeneous flow with relatively flat geometry (Düssler et al. 2022) and are combined with a 2D nozzle geometry close to the trailing edge (see Fig. 2b) to produce spanwise-homogeneous jets. The flow of each fast-acting valve is evenly split to supply four actuation chambers. The flexible tubes connecting the individual components were cut to length so that the supply lines to each actuation chamber had the same total length and pressure loss to ensure spanwise homogeneous flow.

## 2.2 Measurement techniques

In order to quantify the effects of actuation on the airfoil, the global lift  $c_L$ , drag  $c_D$ , and pitching moment  $c_M$  coefficients of the model were measured with an external force balance, the  $c_p$ -distribution was acquired along the airfoil's centerline and for select spanwise positions, and the flow field around the Coandă trailing edge was measured with Particle Image Velocimetry (PIV). The freestream velocity  $U_\infty$  inside the wind tunnel was calculated based on a Prandtl tube at the test section inlet, which also measured the freestream static pressure  $p_\infty$ . At the same location the flow temperature  $T_\infty$  was measured with a Pt100 temperature sensor. The data were acquired as analog input signals with a cRIO 9049 data acquisition system, and LabVIEW FPGA and Real-time 2018 software. For steady cases, a total of 32000 data points were acquired at a frequency of 1.6 kHz for each operating condition.

### 2.2.1 Momentum coefficient

The mass flow for determining  $c_\mu$  according to Eq. 1 was measured with mass flow meters (Testo 6442). The pressure upstream of the mass flow meters was controlled and recorded with proportional valves (Festo MPPE-3-1/2-10-010-B). The multi-level valves (Matrix OX-891.904C2KK) used for fast mass flow variation were controlled with a digital output signal generated in LabVIEW.

In this work the jet is treated as compressible and the compression process is considered isentropic. To reduce the uncertainty of  $c_\mu$  according to Semaan (2020), the following expression for the jet velocity is used:

$$v_{\text{jet}} = \sqrt{\frac{2\gamma RT_t}{\gamma - 1} \left( 1 - \left( \frac{p_\infty}{p_t} \right)^{\frac{\gamma-1}{\gamma}} \right)} \quad (2)$$

where  $\gamma$  is the heat capacity ratio,  $R$  the gas constant,  $T_t$  the total temperature, and  $p_t$  the total pressure. For both upper and lower jet, three of the twelve actuation chambers are equipped with absolute piezo-resistive silicon pressure sensors (Honeywell HSCDRNN030PAAA5) and Pt1000 temperature sensors (B+B sensors F 0,3 (Class B) DIN EN 60751) at a flow stagnation point to measure total pressure  $p_t$  and temperature  $T_t$ , respectively.

### 2.2.2 Pressure measurements

The static pressure distribution along the airfoil chord was acquired with forty-four relative piezo-resistive silicon pressure sensors (thirty-five Honeywell HSCDRRN010NDAA5, nine Honeywell HSCDRRN001PDAA5) and six miniature pressure transducers (Kulite XCE-093-1psiD) on the Coandă surface. Figure 2a shows the pressure sensor distribution along the chord. All sensors were installed close to the airfoil's surface with maximum connecting tube lengths of around 10 mm for the Honeywell and 25 mm for the Kulite sensors. Together with the natural frequencies of  $> 1$  kHz for the Honeywell and  $> 100$  kHz for the Kulite sensors, the frequency response was sufficiently high to resolve the fast pressure fluctuations during unsteady jet actuation. It is noted that the relatively large dimensions of the Honeywell silicon pressure sensors and reduced availability of the Kulite sensors prevented instrumentation of the thin actuator lips.

### 2.2.3 Force measurements

Lift, drag, and pitching moment were measured with an external force balance located underneath the wind tunnel floor. The six-component balance is equipped with seven force transducers (HBM Z6FC4) and their signals are amplified with an MGCplus amplifier. As the balance was not originally designed for full-wing measurements, it was combined with a linear bearing system to protect its most sensitive force transducers from overloading. The bearings effectively reduced the model degrees of freedom to the relevant lift, drag, and pitching moment components. The upper end of the model was fitted with a 3D-printed tip section, visible in the upper part of the zoomed-in view in Fig. 1. This tip section reduced the gap height between model and wind tunnel ceiling to about 2.1 mm, allowing force measurements from the bottom side of the model while minimizing 3D flow effects.

### 2.2.4 Particle image velocimetry

The flow field around the trailing edge of the airfoil was captured with 2C-2D (two-component two-dimensional) time-resolved PIV measurements. The PIV system consisted of high-speed cameras (Phantom v611 and v711) with a resolution of  $1280 \text{ px} \times 800 \text{ px}$  each and a dual-cavity Litron LDY 304 Nd:YLF high-speed laser with a pulse energy of 20 mJ at a repetition rate of 1 kHz. The flow inside the wind tunnel was seeded with DEHS (Di-Ethyl-Hexyl-Sebacate) droplets of  $< 1 \mu\text{m}$  diameter that were produced by two 32-Laskin nozzle seeding generators. To capture the wake region as well as the jet behavior close to the trailing edge two different camera setups with two different fields of view (FOV) were used. Camera setup A comprised two cameras that were mounted side-by-side on top of the test section looking down onto the trailing edge of the vertically mounted model. Both cameras were equipped with  $f = 100 \text{ mm}$  Zeiss Makro Planar T lenses. This setup with merged FOVs of the two cameras expanded the total FOV to  $250 \text{ mm} \times 285 \text{ mm}$ , covering the rear  $22\%c$  of the airfoil and  $28\%c$  downstream of it, as illustrated in Fig. 4a. Camera setup B only comprised a single camera equipped with a  $f = 180 \text{ mm}$  Tamron SP AF Macro lens. This setup captured a zoomed-in perspective of the trailing edge of  $95 \text{ mm} \times 60 \text{ mm}$ , which covered the rear  $8\%c$  of the airfoil and  $11\%c$  downstream of it, as illustrated in Fig. 4b.

The laser beam was introduced into the test section about 1.3 m downstream of the model and formed into a horizontal light sheet of about 2 mm thickness 635 mm above the wind tunnel floor and 15 mm below the airfoil's centerline. This slight displacement of the light sheet with respect to the vertical centerline of the model was chosen to avoid increased light scattering on the pressure taps located on the Coandă trailing edge. The separation time between the two individual laser pulses was set to  $\Delta t = 25 \text{ s}$  for Camera setup A and

$\Delta t = 9 \text{ s}$  for Camera setup B to obtain a pixel shift of about 7 px in both setups. Experiment timing, data acquisition, and processing were done using LaVision's Davis 8.4 software.

A parametric study was carried out to find the optimal processing settings for properly resolving the highly dynamic flow field in the airfoil's wake during impulsive jet actuation. The particle images were processed with a multi-pass cross-correlation algorithm with decreasing interrogation window size. The final passes used a window size of  $16 \text{ px} \times 16 \text{ px}$  and an overlap between neighboring windows of 75%. Additionally, the shape and orientation of the interrogation windows was automatically adapted to the local seeding density and velocity gradients during the last iteration of the final pass to achieve the highest possible accuracy and spatial resolution.

A total of 3000 image pairs were recorded and time-averaged for the steady flow fields presented in this work.

### 2.2.5 Detachment angle on the Coandă surface

The camera setup B of the PIV measurements allows flow field measurements in the vicinity of the trailing edge and estimation of the flow detachment point on the Coandă surface. The detachment is defined here as the point where the local velocity vector is oriented perpendicular to the Coandă surface and has a positive velocity component in freestream direction. The corresponding detachment angle  $\theta$  is the angle between the slot location and detachment point along the elliptical surface, as sketched in Fig. 5a.

The reflections of the PIV laser on the trailing edge prevent measurements of the detachment point directly on the Coandă surface. On the other hand, the resolution of the implemented pressure taps on the Coandă surface is not sufficiently high to enable a temporally- and spatially-accurate prediction of the detachment point. Therefore, the detachment point is approximated based on the local flow field

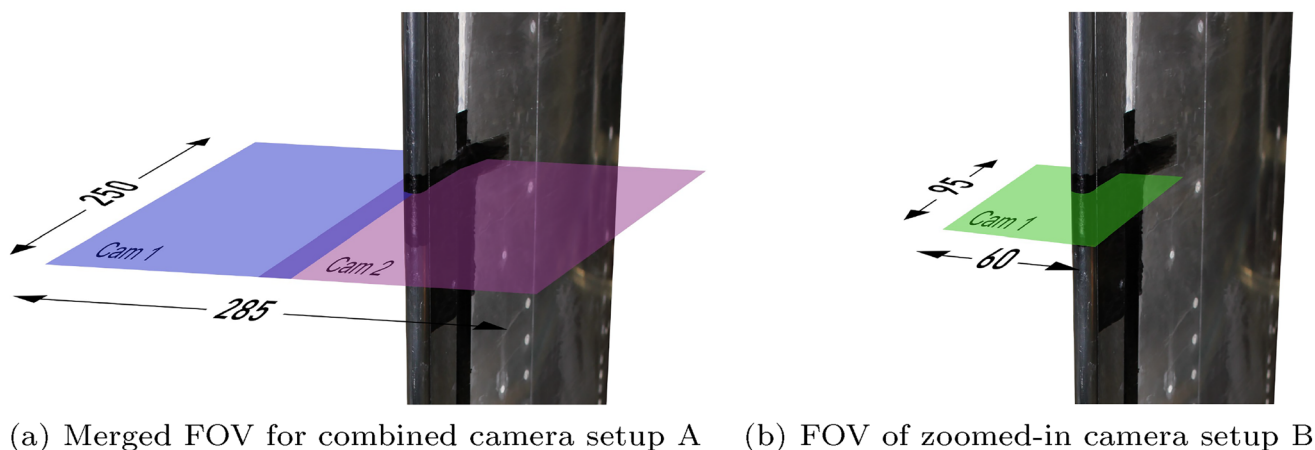
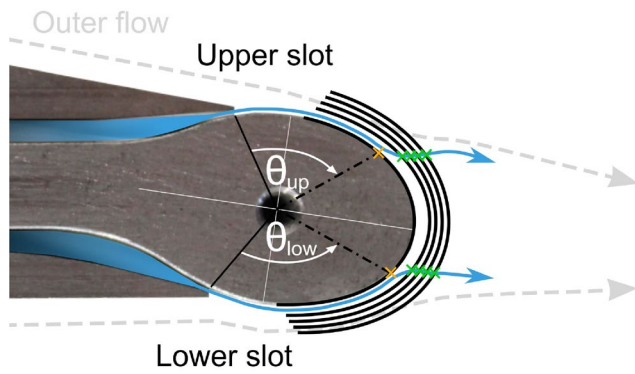
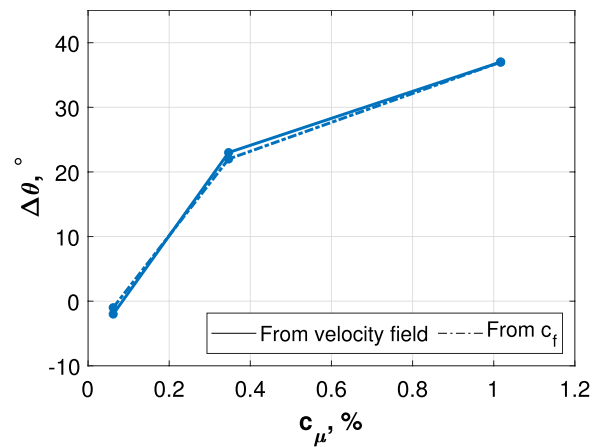


Fig. 4 Sketch of PIV measurement locations on the circulation control airfoil



(a) Detachment angle definition on Coandă surface



(b) Change in detachment angle for two different methods, applied to RANS data

Fig. 5 Principle and validation of detachment angle calculation

angles along four elliptical curves that are centered on the Coandă ellipse and feature wall-normal distances between  $0.2\%c$  and  $0.35\%c$ , as sketched in Fig. 5a. For each of the four curves, detachment angles are determined and then linearly extrapolated onto the Coandă surface.

The methodology is validated with 2D Reynolds-Averaged Navier–Stokes (RANS) simulations, conducted with the TAU code from the German Aerospace Center (DLR). A second order central scheme is applied for spatial discretization and turbulence is modeled with the Spalart–Allmaras negative formulation. The jet and entrained outer flow experience high curvature on the elliptical surface at the trailing edge. For this reason, the rotation and curvature correction (SARC) was applied to the computationally efficient SAneg turbulence model (Spalart and Shur 1997). The SARC model has been validated against experimental data in previous studies as Radespiel et al. (2009) and Swanson et al. (2005). A hybrid computational grid with about 1 million elements was used, including local refinement around the actuator locations and wall-normal resolution that ensured  $y^+(1) \leq 1$ . The mesh is selected by a mesh independence study on the unactuated airfoil. Three grids with different grid density are compared, where both the wall-normal and wall-tangential spacing is uniformly refined by a factor of two between grids. With the Grid Convergence Index, the Richardson extrapolation value is calculated for the lift coefficient, resulting in a difference of 0.32% between the result of the medium grid and the asymptotic solution. For this reason the medium grid is selected for this study. Further details on the numerical setup can be found in Asaro et al. (2021).

The RANS simulations allow comparison of detachment angles calculated from the velocity field via the methodology described above and from the skin friction coefficient  $c_f$  on the Coandă surface. For the second method, the

separation location is identified as the point on the surface where  $c_f = 0$ . This surface location is then converted into the corresponding separation angle  $\theta$ , as indicated in Fig. 5a. A comparison of the results of these two methods is given in Fig. 5b, where the detachment angles are estimated for three different blowing rates from the lower slot. The results are plotted as differences with respect to the detachment angle of the unactuated airfoil. Overall, the two methods show good agreement, with maximum deviations of about  $1^\circ$ . The present methodology is applied to the PIV data and the results are described in Sec. 3.1).

### 2.2.6 Proper orthogonal decomposition

The PIV data are analyzed using proper orthogonal decomposition (POD) analysis. In particular, the snapshot POD method (Sirovich 1987) is applied, where every acquired image is treated as a snapshot of the flow and the mean value is subtracted from them. The flow field is decomposed in a number of spatial modes matching the number of snapshots available, whereby smaller mode numbers contain the largest and hence most energetic flow structures. The identifications of the first modes allow to produce reduced order models that contain the majority of the flow energy.

The relative contribution of each mode to a particular snapshot is represented with a time-varying coefficient. The evolution of these coefficients in time can be analyzed with fast Fourier transformation to identify possible characteristic frequencies. The method proposed by Welch (1967) is used with twenty intervals and 50% overlap in the frequency domain. The POD analysis is applied to measurements of quasi-steady actuator settings and employs the complete data-set of 3000 acquired snapshots each.

### 2.3 Uncertainty and repeatability

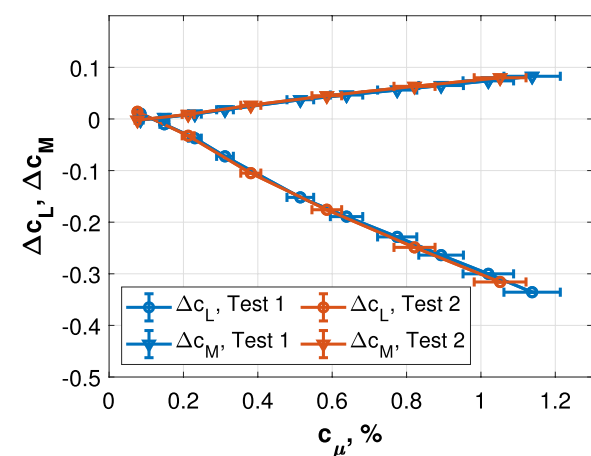
The random ( $s_{\bar{X}}$ ) and systematic ( $b_{\bar{X}}$ ) standard uncertainty of the measurement hardware employed in this work are listed in Table 2. The random uncertainty is calculated from the measured standard deviation and number of samples, while the systematic uncertainties are taken from the manufacturers' specification sheets of the measurement instruments. The table reports the highest uncertainties experienced as percentage values relative to the mean measurement values ( $\bar{X}$ ) encountered during the tests. The nomenclature proposed in ASME (2006) is followed here.

The coefficients of force, moment, pressure, and momentum are not measured directly, but computed from other quantities. Both types of uncertainties are propagated to the derived coefficients based on a first-order Taylor expansion. All uncertainties given in this study are combined uncertainties with  $\delta\bar{X} = \sqrt{s_{\bar{X}}^2 + b_{\bar{X}}^2}$  and reported with a 95% confidence level, i.e. in a  $\pm 1.96\delta\bar{X}$  interval.

An example for typical obtained uncertainties and repeatability of measurements is given in Fig. 6. The two graphs

**Table 2** Random ( $s_{\bar{X}}$ ) and systematic ( $b_{\bar{X}}$ ) standard uncertainty for applied measurement systems

Measurement technique	$s_{\bar{X}}/\bar{X}, \%$	$b_{\bar{X}}/\bar{X}, \%$
Mass flow meters	$9.1 \cdot 10^{-3}$	3.2
Temperature sensors	$8.0 \cdot 10^{-5}$	$5.9 \cdot 10^{-2}$
Pressure transducers	$3.3 \cdot 10^{-7}$	$1.7 \cdot 10^{-3}$
Force balance	1.1	1.8
PIV	0.2	1.5

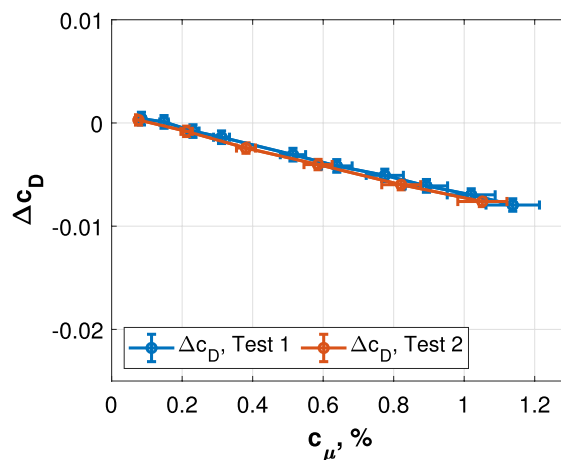


(a) Lift and pitching moment coefficients for different levels of lower slot blowing

depict changes of lift coefficient  $c_L$ , pitching moment coefficient  $c_M$  and drag coefficient  $c_D$  relative to the unactuated operating condition and as a function of momentum coefficient  $c_\mu$  for different levels of lower slot blowing. The graphs include the corresponding measurement uncertainties as error bars with  $\bar{X} \pm 1.96 \delta\bar{X}$ . One can see that the load coefficients feature negligible measurement uncertainty, while the uncertainty in momentum coefficient is more pronounced, particularly for high levels of  $c_\mu$ . The figure further includes data from measurements with the same operating conditions, but acquired on different days towards the beginning and end of the test entry, highlighting measurement repeatability. Furthermore examples for measurement uncertainties are present in Fig. 11 for the pressure coefficient  $c_p$  and in Fig. 22 for  $c_L$  values during unsteady actuation of the jets.

### 2.4 Slot height and jet velocity distribution

Prior to the wind tunnel test, the slot heights were adjusted with push- and pull-screws and measured along the airfoil's span with a laser scanner and a flattened Pitot tube. The sensors were automatically moved along the span on a traverse with a stepper motor. Figures 7a and d show the slot height distributions for the upper and lower jet, respectively, outside the tunnel, both with and without blowing. The adjusted slots featured a slightly increased average slot height compared to the target value of  $0.08\%c$  with span-wise slot height distributions of  $h_{lw} = 0.086\%c \pm 0.0056\%c$  ( $\pm 6.4\%$ ) and  $h_{up} = 0.082\%c \pm 0.0055\%c$  ( $\pm 6.8\%$ ) for the lower and upper slot, respectively. The measured slot heights for different actuation states indicate that the lip design was rigid enough to prevent significant changes in slot height during actuation and wind tunnel testing.



(b) Drag coefficient for different levels of lower slot blowing

**Fig. 6** Uncertainty and repeatability of measurements on different days



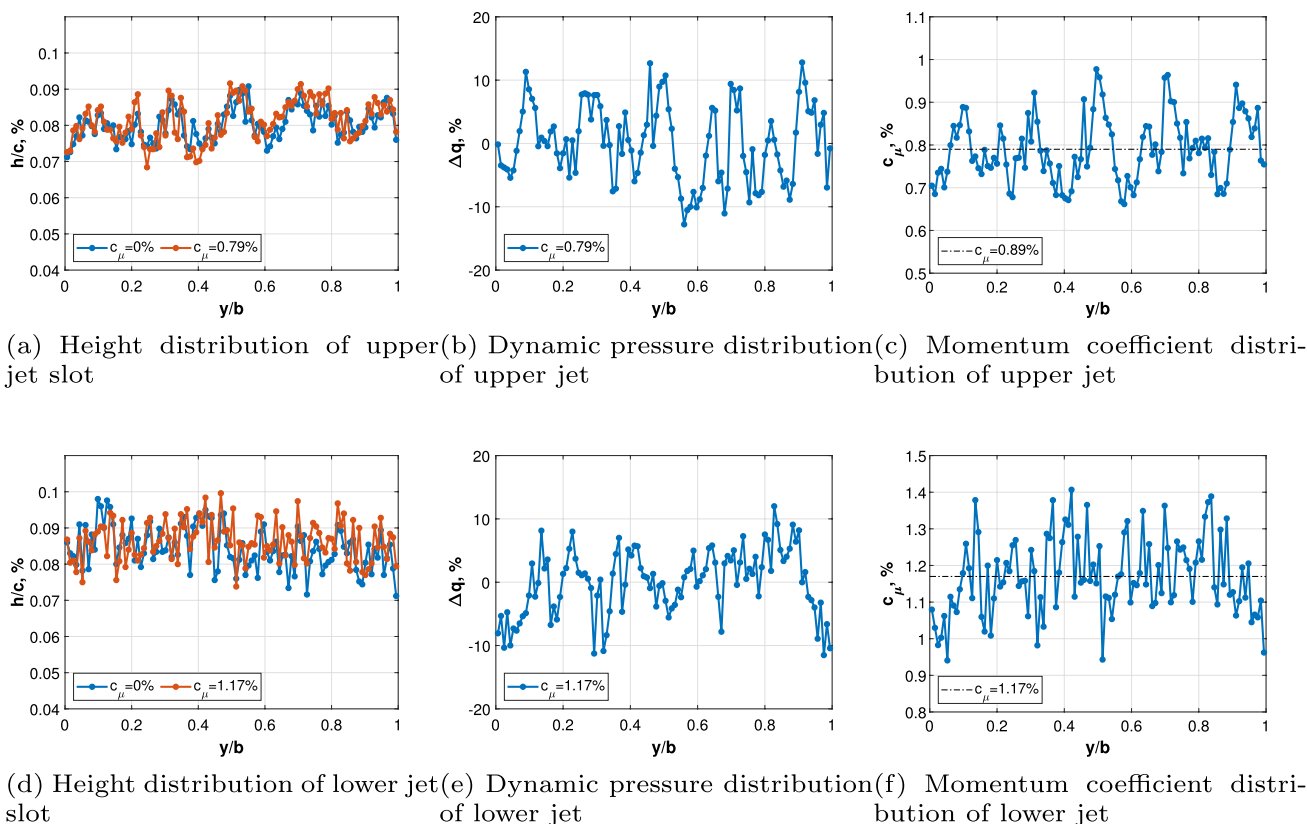


**Fig. 7** Distributions of slot height  $h$ , jet dynamic pressure  $q$  and  $c_\mu$  of upper and lower jet along span  $b$

Figures 7b and e show the corresponding variation in dynamic pressure  $\Delta q$  of the jet sheets along the span at maximum blowing rates for upper and lower jet, respectively. The total pressure is measured with a flattened Pitot tube on the Coandă surface 0.8%  $c$  downstream of each slot location. The plots show the percentage variation of dynamic jet pressure relative to the mean value:

$$\Delta q(y) = \frac{q(y) - \bar{q}}{\bar{q}} \cdot 100, \tag{3}$$

where  $q$  indicates the local dynamic pressure at spanwise position  $y$  and  $\bar{q}$  the average dynamic pressure along the span. The standard deviation of  $\Delta q$  is 5.1% for the lower slot and 6.1% for the upper slot. The obtained results are in line with previously characterized slot geometries, e.g. Düssler et al. (2022).

The local variation of  $c_\mu$  along the span is exceedingly difficult to determine accurately and, to the authors' knowledge, has not been documented in any other previous paper on circulation control. An attempt is made here to characterize the spanwise distribution of  $c_\mu$  based on the measured variation in slot height  $h$  and dynamic pressure  $q$ . Assuming that the measured dynamic pressure is indeed directly proportional to the jet velocity  $v_{jet}$  at the jet's throat and that

compressibility only has a small impact on this, the local momentum coefficient is approximated as  $c_\mu \propto v_{jet}^2 \cdot h$ . It is noted that the distribution is scaled to reproduce the average value of  $c_\mu$  across the entire span, which is based on precise acquisition of total jet mass flow. The corresponding distributions are presented in Fig. 7c and f. The upper jet features a standard deviation of 9.6% and the lower jet of 9% for the momentum coefficient.

### 3 Results

The following section is split into the analysis of steady results (Sect. 3.1) and unsteady results, i.e. time-resolved data for impulsive jet actuation (Sect. 3.2). The steady results illustrate airfoil performance for single upper and lower slot blowing, and dual blowing with simultaneous and differential blowing from both slots. Actuation effects on the flow field around the trailing edge are analyzed.

Example results are presented for the impulsive activation and deactivation of the blowing system. All force coefficients reported herein are given as differences to the unblown case, e.g. as  $\Delta c_L = c_{L,blown} - c_{L,unblown}$  and accordingly for  $\Delta c_D$  and  $\Delta c_M$ . The pitching moment coefficients are

calculated with respect to the quarter chord line. If not specified otherwise, the results correspond to an angle of attack of  $\alpha = 0^\circ$ . In order to estimate wind tunnel effects for steady operation of the current circulation control airfoil, a corresponding angle of attack correction for a 2D airfoil model in a closed, rectangular test section is calculated according to Ewald (1998):

$$\Delta\alpha = \frac{\pi c^2}{96\beta H^2} (c_L + 4c_M) \quad (4)$$

where  $\beta$  is the Prandtl-Glauert compressibility factor and  $H$  the tunnel height. Here, the lift and pitching moment coefficients of the actuated airfoil are applied and the higher order term  $(c/H)^4$  is not included, since  $c < 0.4\beta H$ . Figure 8 shows the calculated angle of attack correction  $\Delta\alpha$  for the different combinations of upper and lower steady blowing investigated in this study. As expected, the correction values scale with the magnitude of the blowing and the consequent change in lift coefficient, taking on values of up to  $\pm 0.5^\circ$ . This means that the blowing performance obtained in the wind tunnel experiment is slightly overpredicted compared to operation in unbounded flow. The correction of wind tunnel effects for dynamically actuated circulation control airfoils is non-trivial and currently under investigation. For better comparability between steady and unsteady results, the corrections are not applied to the steady results, but reported here for reference, similarly to Jones (2005).

### 3.1 Steady actuator performance

The evolution of lift  $\Delta c_L$ , drag  $\Delta c_D$ , and pitching moment  $\Delta c_M$  coefficients relative to the unactuated airfoil values are plotted as a function of momentum coefficient  $c_\mu$  for different combinations of single and dual blowing in Fig. 9.

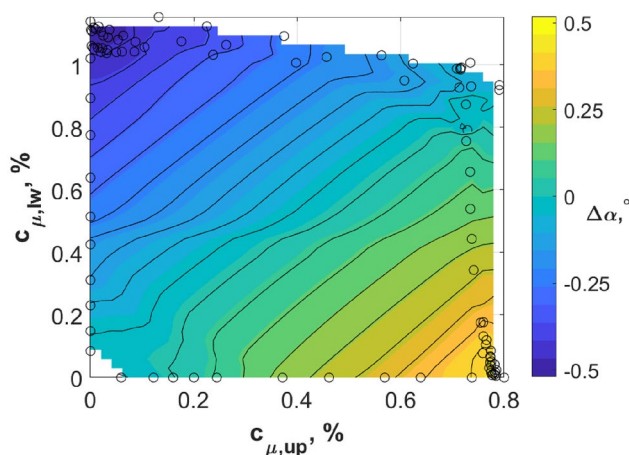


**Fig. 8** Angle of attack correction for the tested steady blowing conditions

The graphs feature a variation of blowing from zero to  $c_{\mu,up} = 0.80\%$  for the upper and zero to  $c_{\mu,lw} = 1.13\%$  for the lower jet. The actual measurement points are marked by black circles in the graphs. In addition, a linear regression model is used to interpolate the force and moment coefficients inside the experimentally acquired data point range, which is plotted as a colored contour plot including black isolines. The left and lower edges of the contour plots represent cases where only one of the two jets is active. For the dual blowing cases, one of the two jets is kept at near-constant and relatively high  $c_\mu$ , while the other jet is varied in strength up to about the same blowing level. For near-constant upper blowing, the lower blowing is increased from 0 to 55% of the combined total momentum coefficient  $c_{\mu,tot}$ , while for constant lower blowing the upper blowing is varied from 0 to 42%  $c_{\mu,tot}$ . It is worth noting that the applicability of the linear regression between data points was checked in a follow-up experiment with a more uniform distribution of data points over the presented parameter space. The general trends found in this second experiment matched the ones predicted here based on the linear regression approach. Due to differences between the two experimental setups, however, the additional data points have not been incorporated in Fig. 9.

The lift coefficient differences exhibit a close-to-linear dependency on  $c_\mu$  for both single and dual blowing, apart from a small non-linearity for very low blowing rates, as shown in Fig. 9a. The circulation control airfoil has the capability to independently increase and decrease the lift in a range from  $\Delta c_L = -0.34$  to  $\Delta c_L = 0.33$ . The pitching moment coefficient in Fig. 9b features a trend similar to the lift coefficient, but with opposite sign, i.e. increasing lift decreases pitching moment and vice versa. The drag coefficient graph in Fig. 9c shows that the tangential blowing reduces airfoil drag with a close to linear trend, for both single and dual blowing. In addition, the number of POD modes needed to represent a certain fraction (80%) of the total kinetic energy in the wake is also plotted in Fig. 9d. This measure gives an indication of the size of dominant flow structures in the flow, with a smaller number of modes indicating dominantly larger flow structures and vice versa. The number of required POD modes increases with total blowing rate and reaches its maximum for the conditions corresponding to minimal drag. This finding is not surprising, as the corresponding large number of POD modes indicates the presence of small flow structures and absence of large-scale vortex shedding, thereby indicating a smaller and more steady airfoil wake. A more detailed analysis of POD results, including a comparison of the first POD modes for different blowing levels, will be given in Figs. 15 and 16 later in this paper.

Starting at moderate blowing rates of  $c_\mu \geq 0.4\%$ , upper and lower slot blowing exhibit asymmetric behavior, as

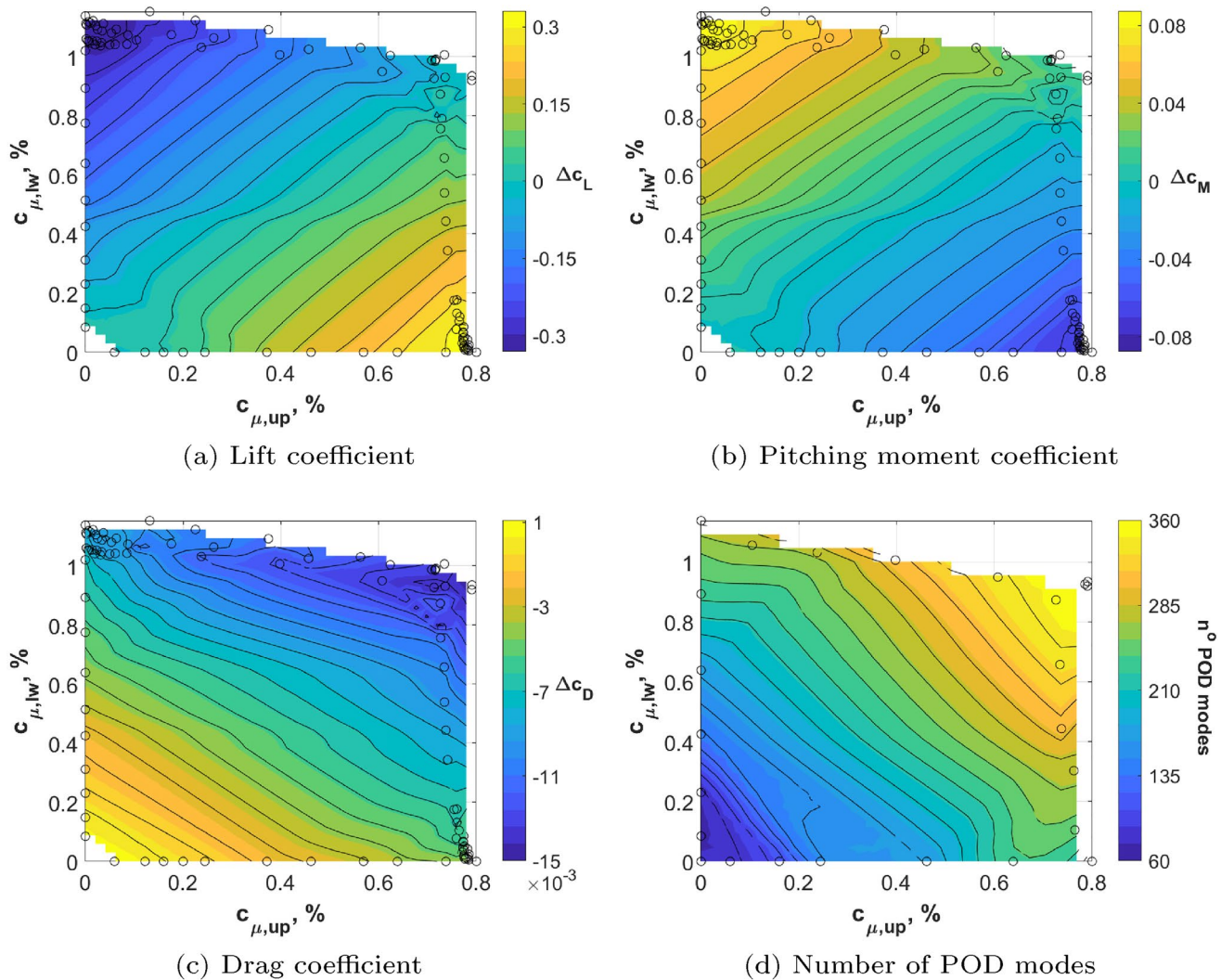


**Fig. 9** Load changes for different combinations of steady upper and lower slot blowing and number of POD modes required to represent 80% of energy

upper blowing requires lower  $c_{\mu}$  to obtain the same absolute lift change as lower blowing. While the values of maximum lift change of upper and lower blowing are similar in magnitude, the lower jet requires about 40% higher  $c_{\mu}$  to achieve this. This asymmetry in lift control authority is likely attributed to the asymmetry of the airfoil that leads to an asymmetric integration of the actuator geometry into the airfoil’s cambered trailing edge. Asymmetry is also observed for the drag coefficient and blowing with  $c_{\mu} \geq 0.4\%$ , where lower blowing leads to reduced drag values compared to upper blowing at similar  $c_{\mu}$ .

For dual blowing, the lift and pitching moment coefficients approach the unactuated values for equal blowing from upper and lower slot. Unlike for single blowing, the lift coefficient change for blowing ratios away from

this equilibrium line features a slightly non-linear trend. The corresponding drag coefficients are in general lower compared to single blowing.

The results highlight the close-to-linear steady actuation behavior of the single and dual slot jets. The lift and pitching moment are coupled, similarly to the aileron. Correspondingly, compensating the full wing pitching moment would only be possible with a secondary actuator. The asymmetry of upper and lower blowing is also reflected in the ability of both jets to suppress vortex shedding from the blunt trailing edge.

Another way to analyze the performance of the blowing system is through the ratio of lift change to equivalent drag change, defined as:

$$\frac{|\Delta c_L|}{\Delta c_{D,e}} = \frac{|\Delta c_L|}{\Delta c_D + c_\mu} \tag{5}$$

where the differences with respect to the unactuated case are considered instead of the absolute values. Compared to the lift-to-drag ratio, the present expression also takes into account the work done on the fluid in order to produce the pressurized air jet, which takes on the form of an additional drag component. Figure 10 compares the performance of single and dual blowing in terms of the ratio of lift change to equivalent drag change (Fig. 10a) and lift change to pitching moment change  $|\Delta c_L/\Delta c_M|$  (Fig. 10b), both as a function of the realized lift coefficient change  $\Delta c_L$ . The graphs therefore indicate how efficiently a specific lift change can be realized and how close the coupling is with the pitching moment.

The left half of both graphs features predominantly lower slot blowing and the right half predominantly upper slot blowing. For dual blowing cases where the opposite jet is activated with  $\leq 14\%c_{\mu,tot}$ , as present in the outermost data points in Fig. 10a, the equivalent drag is reduced relative to single blowing with comparable lift coefficient change. Correspondingly, these cases feature an increased lift-to-equivalent-drag ratio change and therefore increased performance. This effect is more pronounced for predominant lower and marginal upper blowing, located on the left side of the graphs. This hints at the possibility to improve airfoil performance with dual slot blowing despite the marginal effect on lift change rate alone.

The lift-to-pitching-moment ratio change shown in Fig. 10b is a measure of how closely coupled the actuator-induced changes in lift and pitching moment coefficients are. Higher values indicate reduced changes in pitching moment for a given lift change, which are desirable for typical

applications. The lift-to-pitching-moment ratio change is relatively constant for single blowing at higher blowing rates and approaches the dual blowing values for reduced opposite jet operation towards the left and right side of the graph. The upper side blowing features higher values and therefore a desirable smaller impact on pitching moment. The dual blowing curves indicate a non-linear relationship between lift and pitching moment, which becomes more pronounced for increased total blowing rates towards the center of the graph. This highlights the possibility to decouple lift and pitching moment and obtain some level of independent control for cases that do not require peak lift change magnitudes. Dominant lower slot blowing combined with increasingly strong upper blowing leads to stronger coupling between lift and pitching moment, whereas dominant upper blowing with increasingly strong lower blowing leads to reduced coupling between the two coefficients.

The surface pressure distributions for different levels of single slot blowing are shown in Fig. 11 for upper (a) and lower (b) blowing. It is noted that the pressure signals feature a slight disturbance close to the  $x = 5\%c$  location where a zig-zag tape was added for transition fixation. Dashed lines connecting the pressure sensors on the main part of the airfoil and Coandă surface are added only as a guide to the eye. As mentioned before, no pressure transducers could be implemented in this region due to the unavailable space inside the model. Consequently, the lift and pitching moment coefficients were calculated without taking contributions from this part of the airfoil into account. Based on CFD simulations of this airfoil inside the wind tunnel with matching blowing conditions, the contribution of this part of the airfoil to the lift coefficient amounts at most to 0.02 for maximum upper blowing.

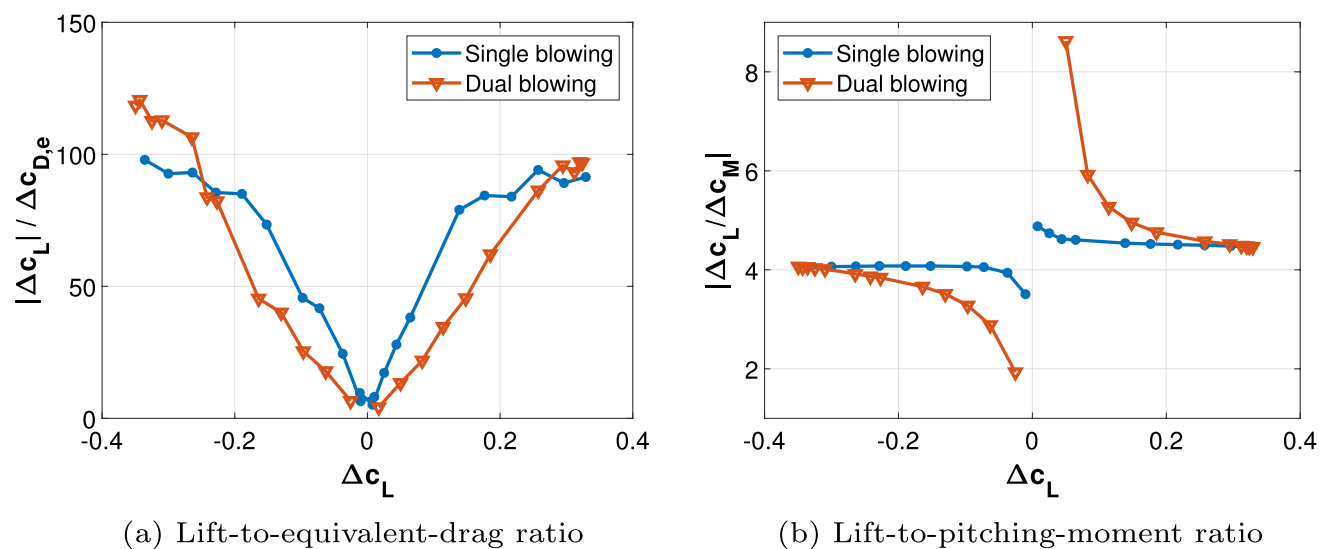


Fig. 10 Change in lift-to-equivalent-drag and lift-to-pitching-moment ratios for single and dual blowing

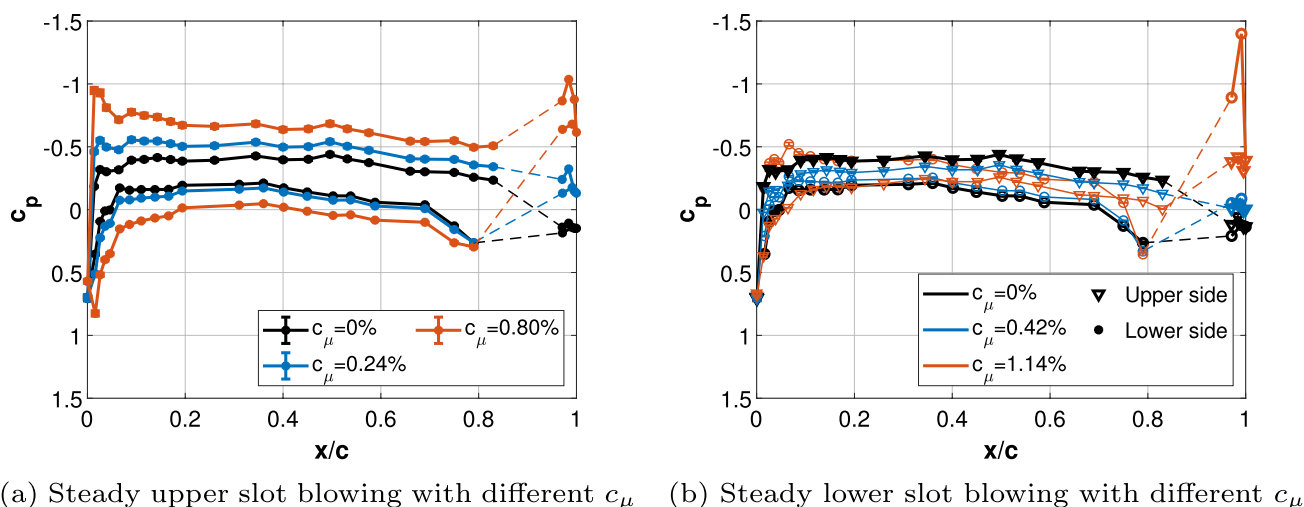


Fig. 11 Pressure distribution along the airfoil center section for different levels of single slot blowing

Upper blowing leads to an increased enclosed area between the pressure curves on pressure and suction side and consequently higher lift. Increasing blowing leads to the formation of a pronounced suction peak. For lower blowing, the area between the two curves reduces with increasing  $c_{\mu}$ . For peak lower blowing, the pressure difference between upper and lower airfoil side reverses in the front part of the airfoil, making the pressure distribution on the lower side resemble the pressure distribution on the upper side without blowing and vice versa. The airfoil with maximum lower blowing therefore produces downforce from the leading edge to around  $x \approx 75\%c$  and on the Coandă surface. For intermediate levels of upper blowing ( $c_{\mu,up} = 0.24\%$ ), the change in pressure on the upper side is responsible for 75% of the total lift change with respect to the unactuated airfoil. For peak upper blowing, this contribution slightly reduces to 69%, still showing that the dominant impact of upper slot actuation occurs on the upper side. For intermediate levels of lower blowing, again the lift change is mostly driven by the pressure change on the upper side (67% of total), but contributions become nearly balanced (48%) between upper and lower side for peak lower slot blowing. The impact of the local pressure changes at the Coandă surface on the total lift is below 4.1% (for maximum lower blowing) and therefore insignificant. For increasing levels of jet actuation, the pressure-based lift coefficient changes at the airfoil's centerline are increasingly higher than the global values determined by force balance, reaching a maximum deviation of 13.1% for peak lower blowing.

This difference between local and global lift coefficient indicates that there are residual 3D flow effects present on the model, e.g. due to interactions with the wind tunnel floor and ceiling and reduced blowing homogeneity close to the ends of the blowing slots. This is confirmed by observing

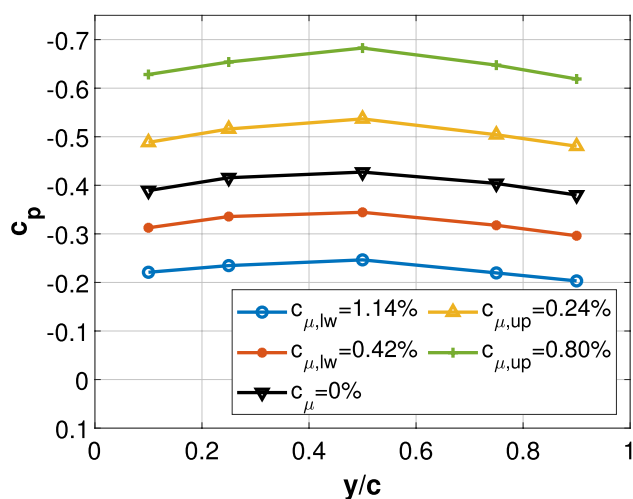
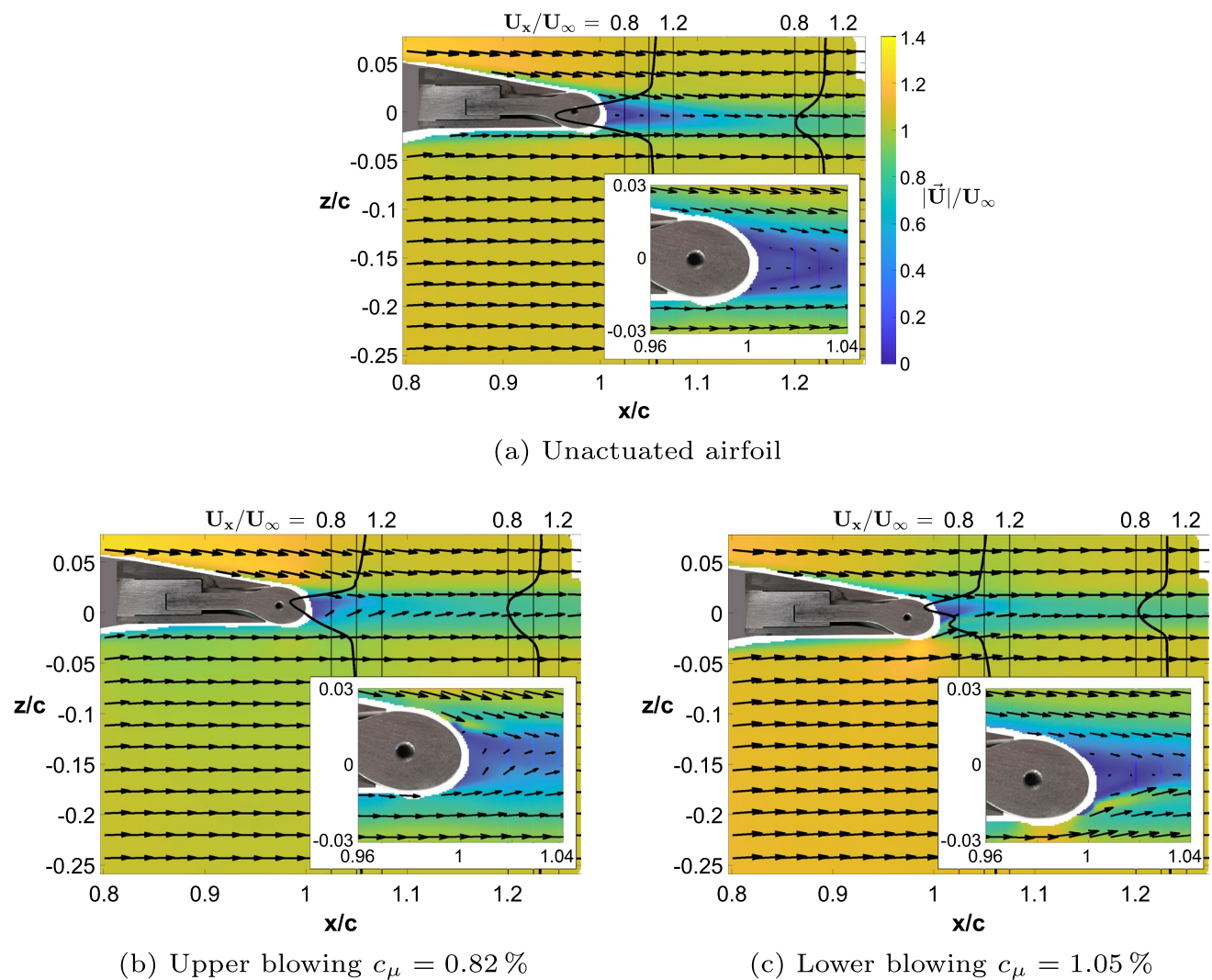


Fig. 12 Spanwise distribution of  $c_p$  on upper side at  $x/c = 0.4$

the spanwise pressure distribution along the model's suction side at  $x/c = 0.4$ , which is shown in Fig. 12 for different levels of upper and lower slot blowing. Correspondingly, the spanwise lift distribution also features its peak lift change in the model's centerline and reduced values towards the walls, effectively reducing the global lift coefficient.

The cases of peak upper and lower slot blowing (orange lines in Fig. 11) are analyzed in more detail here based on the actuator-induced changes of the flow field downstream of the airfoil. Figure 13 shows the time-averaged flow field around the airfoil's trailing edge, with insets displaying zoomed-in sections around the Coandă surface, based on the reduced field of view sketched in Fig. 4b. Different blowing conditions are compared here, with the unactuated airfoil shown in Fig. 13a, maximum upper blowing with  $c_{\mu} = 0.82\%$  in



**Fig. 13** Flow fields around trailing edge for different blowing conditions

Fig. 13b, and maximum lower blowing with  $c_\mu = 1.05\%$  in Fig. 13c. The contour plots of the velocity magnitude are normalized with  $U_\infty$  and only one in 196 velocity vectors is shown for clarity. In the larger field of view black curves depict vertical profiles of the horizontal velocity component  $U_x$  at positions  $x = 1.05c$  and  $x = 1.22c$  downstream of the airfoil. The velocity field around the unactuated airfoil features a pronounced deficit in velocity magnitude directly downstream of the blunt trailing edge, as well as increased flow velocities on the suction side. Both single blowing cases change the shape of the separated flow region on the Coandă surface, reducing the overall velocity deficit in the wake. Upper slot blowing leads to an increase in velocity magnitude on the suction side of the airfoil. Lower slot blowing leads to increased velocity magnitude on the pressure side and high local flow velocities on the lower side of the Coandă surface, reducing lift. The wake is deflected

upwards and the separated flow region moves upwards as well. For relatively high momentum coefficient the jet splits the wake, resulting in a dual-peak wake deficit contour close to the trailing edge. For all cases the wake deficit evens out further downstream through vertical momentum exchange and it reduces from  $\leq 60\%U_\infty$  to  $\geq 80\%U_\infty$  in the observed range. The velocity fields also show the boundary layer, although the resolution is not high enough to resolve it properly because the region close to the wall was masked during processing due to laser reflections.

Based on the methodology introduced in Fig. 5, the effect of blowing on the flow detachment angle on the Coandă surface is analyzed. Figure 14 shows the change in flow detachment angle ( $\Delta\theta$ ) with respect to the unactuated airfoil as a function of the momentum coefficient for both upper and lower blowing. Lower blowing continuously moves the flow detachment point towards the trailing edge with increasing

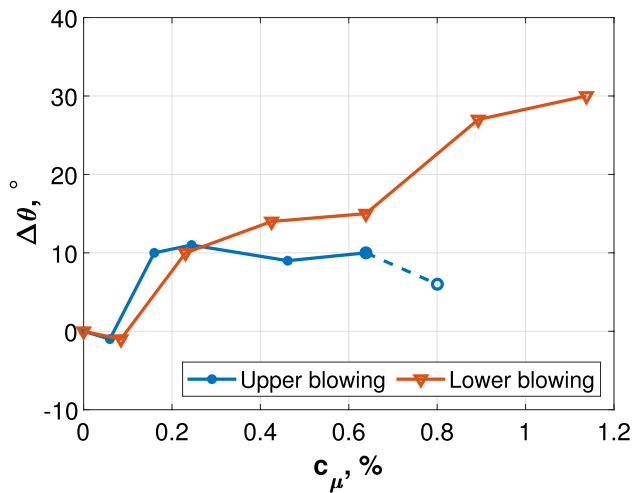


**Fig. 14** Detachment angle change on Coandă surface for different single blowing conditions

$c_\mu$ . For peak lower blowing, the detachment point is shifted aft by about  $\Delta\theta_{lw} = 30^\circ$ . The upper blowing also results in a rearward deflection of the detachment point, but the trend stagnates around  $\Delta\theta_{up} = 10^\circ$  and even features a reversal around  $c_\mu = 0.8\%$ . It is noted that this detachment angle coincides with the position of a pressure tap close to the laser light sheet, which might have impacted the flow field on the upper side of the Coandă surface locally, especially for the marked peak blowing at  $c_\mu = 0.8\%$ . For very small levels of blowing at  $c_\mu \leq 0.1\%$ , both upper and lower blowing result in an earlier detachment with respect to the unactuated airfoil. This trend matches the sign change visible in the lift and pitching moment coefficients in Fig. 6a for very low values of  $c_\mu$  compared to higher blowing levels.

Upper slot blowing at this small level, for example, leads to a very slight lift reduction of  $\Delta c_L = -0.0114$  and a pitching moment increase. A possible explanation for this control reversal effect could be a changed reattachment behavior of the outer flow downstream of the retracted jet outlets, which was observed in CFD data. It is found that a small jet blowing rate reduces the size of the separated flow region downstream of the lip and slot, leading to earlier reattachment of the outer flow onto the Coandă surface. The marginal blowing rate does not add any significant momentum to the boundary layer, but the earlier flow reattachment results in a longer exposure of the flow to the positive pressure gradient along the Coandă surface. The correspondingly occurring increased momentum loss is not compensated by the small additional jet momentum and therefore results in earlier flow separation from the Coandă surface, as shown in Fig. 14 and discussed in more detail by Asaro et al. (2021).

As mentioned above, the PIV dataset was also evaluated based on a POD analysis. An initial result was shown in Fig. 8d, depicting the number of POD modes required to represent 80% of the energy contained in the flow. A further analysis of the POD results reported in Fig. 9d is conducted to identify potential coherent structures in the airfoil’s wake and their modification through steady blowing. Figure 15 depicts the streamwise velocity component of the first, and therefore most energetic, POD modes for different combinations of single and dual blowing. The captions underneath each subplot specify the blowing level and the relative energy content of the first mode in parentheses. The unactuated airfoil (Fig. 15a) exhibits a typical vortex shedding pattern in the wake of the blunt trailing edge, with alternating clockwise and counterclockwise vortices. The onset of blowing leads to a successive reduction in vortex

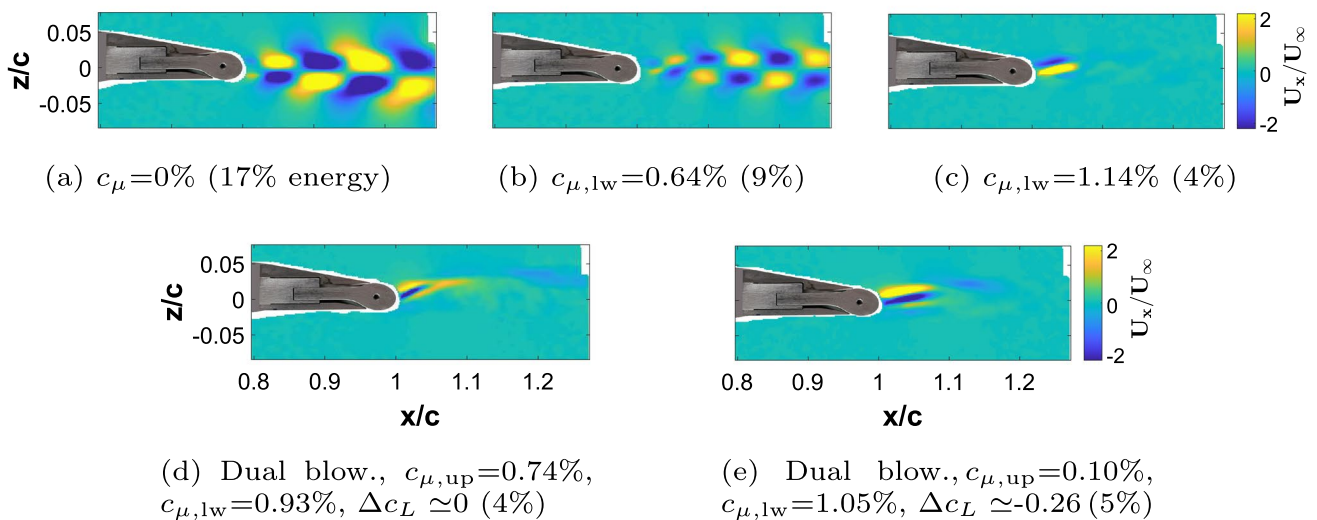


**Fig. 15** First POD modes for different blowing conditions, relative energy of modes given in brackets

size (Fig. 15b), until the vortex shedding is completely suppressed (Fig. 15c). In this case, the dominant mode features the steady air jet and its relative energy content is vastly reduced. Correspondingly, the energy contained in the flow is more evenly distributed over a larger number of modes (see Fig. 9d), indicating the presence of smaller flow structures that also correlate with a reduced wake deficit behind the trailing edge (Fig. 13). Similar effects of blowing on the vortex shedding have been found by El Sayed et al. (2017).

Figures 15d and e depict two cases with dual blowing. In the first one, similar blowing strength is applied from upper and lower slot, leading to a  $\Delta c_L \approx 0$  comparable to the baseline case in Fig. 15a, but with a significantly reduced drag ( $-47\%$ ) due to the suppressed vortex shedding. This case illustrates the benefits of applying steady dual blowing to improve the aerodynamic properties of the modified airfoil. The second dual blowing case in Fig. 15e illustrates the effect of marginal opposite blowing during load alleviation setting, especially in comparison with the single blowing case shown in Fig. 15c. The two cases feature the similar total blowing rate, but the dual blowing in Fig. 15e exhibits higher lift-to-equivalent-drag ratio, as the secondary jet modifies the wake leading to a drag reduction with minimum impact on lift.

The power spectral density of the time coefficient related to the first mode is plotted in Fig. 16 for different levels of lower slot blowing. The corresponding dominant frequencies are highlighted by markers in the plot. The curves feature distinct peaks for moderate blowing rates of  $c_\mu \leq 0.42\%$ , indicating again the presence of vortex shedding from the blunt trailing edge at blowing-dependent frequencies between 234 and 346 Hz. These characteristic frequencies tend towards smaller values with increasing blowing intensity, with the notable exception for the smallest blowing rate at  $c_\mu = 0.084\%$  that shows again an opposite trend. With increasing blowing intensity, the dominant mode switches to a quasi-steady representation of the blowing jet and the corresponding time coefficients do not exhibit a characteristic frequency peak anymore. Similar trend is observed for the upper blowing, here not reported for brevity. The results are in line with the findings in Fig. 15 and illustrate the change in flow topology with increasing blowing strength.

### 3.2 Jet performance for impulsive activation

The activation time of the actuator is crucial for effectively counteracting the loads induced by discrete vertical gusts, especially for relatively short gust lengths and delayed gust detection by onboard sensors. Section 3.1 analyzed the steady control authority of the Coandă actuator, whereas here the impulsive activation and deactivation of the system is explored, similar to how it would be operated to counteract discrete vertical gusts. The shortest gust of

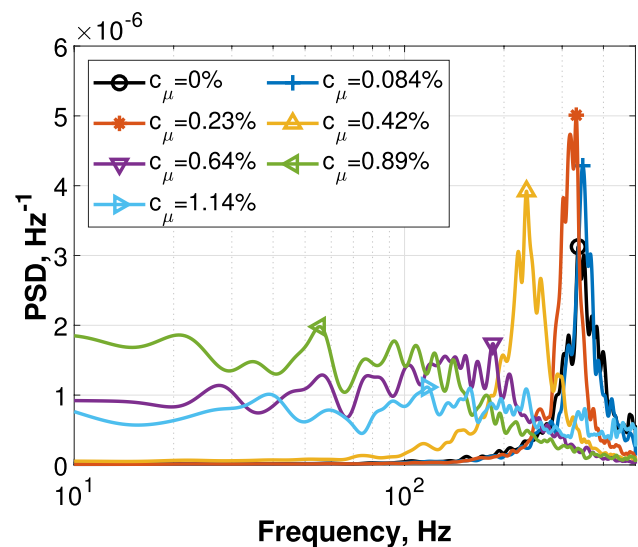
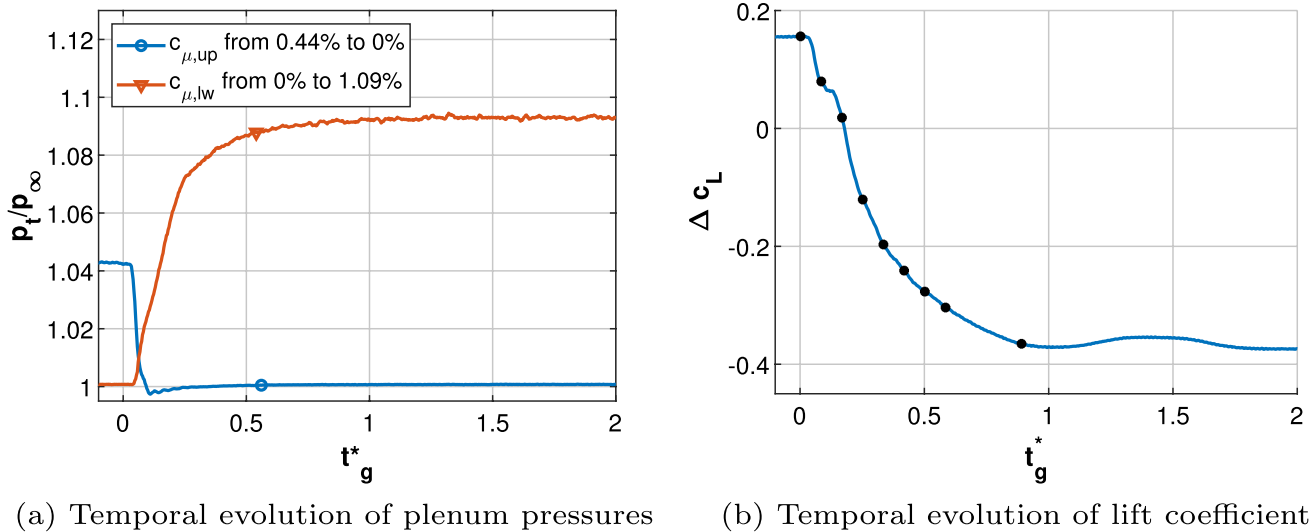


Fig. 16 Power spectral density of first POD mode time coefficient for lower blowing

1-cosine shape defined in EASA's certification documentation (EASA 2020) has a length of 18 m and reaches its peak velocity at the half width  $H = 9$  m. In order to obtain a meaningful quantity for the onset duration of the gust-induced effects, a non-dimensional time is defined here. Unlike the often applied definition of the characteristic time, which is non-dimensionalized with the chord length  $c$  or half chord length  $c/2$  and freestream velocity  $U_\infty$ , here the gust half length  $H$  is chosen as a reference length to define  $t_g^* = t \cdot U_\infty / H$ . A value of  $t_g^* = 1$  corresponds to the time required for the gust-induced changes of the flow field to grow from zero to their respective peak values, or for the freestream to pass over the airfoil  $H/c$  times. For comparison, the value of  $t^*$  calculated with  $c$  is included in brackets. The results presented in this section correspond to ensemble-averaged data based on 20 unsteady actuator switching cycles.

It was found that the force measurements based on the wind tunnel balance displayed significant oscillations around the commanded steady load levels. These are attributed to the impact of accelerations of the model, which was only mounted from one side to enable the force measurements. For this reason, the lift coefficients in this section were obtained by integration of the measured surface pressure distributions along the model's centerline. In comparison, the corresponding global lift coefficients obtained by the force balance are slightly smaller due to the presence of residual 3D flow effects, e.g. from interactions with the wind tunnel ceiling and floor and slightly reduced blowing homogeneity close to the ends of the blowing slots, as highlighted in Fig. 12. The spanwise





**Fig. 17** Temporal evolution of plenum pressures and lift coefficient for impulsive switching from performance restoration to load alleviation

distribution of lift changes  $\Delta c_L$  therefore peaks at the model’s centerline, where quasi-planar (2D) flow occurs.

Figure 17a shows the time course signal of the total pressure ratio  $p_t/p_\infty$  inside the upper and lower plenum chambers for typical impulsive switching of the actuation state. In this example case, the initial condition at  $t_g^* < 0$  features partially open valves for the upper and closed valves for the lower plenum chambers for performance restoration of the airfoil at undisturbed cruise flight. The states of the fast-acting valves are switched simultaneously and impulsively at  $t_g^* = 0$ . The final condition corresponds to gust load alleviation with fully open valves for the lower and closed valves for the upper plenum chambers. The upper plenum shows a slight under-shooting before converging to the steady-state value at  $\Delta t_g^* = 0.56$  ( $\Delta t^* = 10.1$ ), whereas activation of the lower valves requires an onset time of  $\Delta t_g^* = 0.54$  ( $\Delta t^* = 9.72$ ). Both plenum switching times are therefore almost twice times faster than than the fastest gust onset time at ground conditions.

The increase in lower plenum pressure over time leads to the establishment of a tangential air jet over the lower half of the Coandă surface, onset of increased momentum transfer normal to the wall and upwards deflection of the flow downstream of the airfoil, corresponding to an asymptotic decrease in airfoil circulation and lift coefficient, as shown in Fig. 17b. At  $\Delta t_g^* = 0.89$  ( $\Delta t^* = 16$ ), the airfoil reaches 99% of the steady  $\Delta c_L$ , showing a slower reaction time than the pressure in the plenum chambers but still faster than the fastest gust at ground altitude. The switching between upper and lower blowing produces a maximum change in lift coefficient of  $\Delta c_L = -0.52$ . For this example switching sequence, the time evolution of the flow field around the trailing edge

(Fig. 18), wake velocity profile (Fig. 19), and surface pressure distribution (Fig. 20) is analyzed at selected points in time, marked in black in Fig. 17b. A total of nine points in time are selected, eight between  $t_g^* = 0$  to  $t_g^* = 0.58$  in steps of  $\Delta t_g^* = 0.083$  and one at  $t_g^* = 0.89$ , where  $\Delta c_L$  reaches 99% of the steady value.

The change of the flow field around the trailing edge over the course of the impulsive switching sequence from upper and lower blowing is shown in Fig. 18. The flow fields at the first ( $t_g^* = 0$ ) and final ( $t_g^* = 0.89$ ) point in time closely resemble the corresponding flow conditions during steady jet operation at the corresponding blowing conditions. The two cases in between highlight the transient processes taking place. Clearly visible is the increase in flow velocity close to the lower Coandă surface over time and establishment of the lower jet, which is visible as an upwards-directed high-velocity band downstream of the model. With the onset of the jet, the entrainment of outer flow occurs, leading to upwards deflection of flow downstream of the airfoil, which is most apparent on the lower side of the airfoil’s wake. It is also apparent that the wake deficit, indicated by a dark blue region shifts upwards ( $t_g^* = 0.17$ ) before decreasing in size in subsequent time steps.

The switching of the two jets has a direct impact on the airfoil’s wake. For example, Fig. 19 depicts the deficit in horizontal velocity component  $U_x/U_\infty$  at  $x = 1.02c$  for all the selected points in time. At  $t_g^* = 0$ , the wake profile is deflected downwards and the effect of the upper jet is directly visible as added velocity in the velocity distribution in the form of a plateau around  $z/c \approx 0.007$ . This secondary peak is due to the separated jet entering the wake, as also shown in Miklosovic et al. (2016). As the lower jet builds

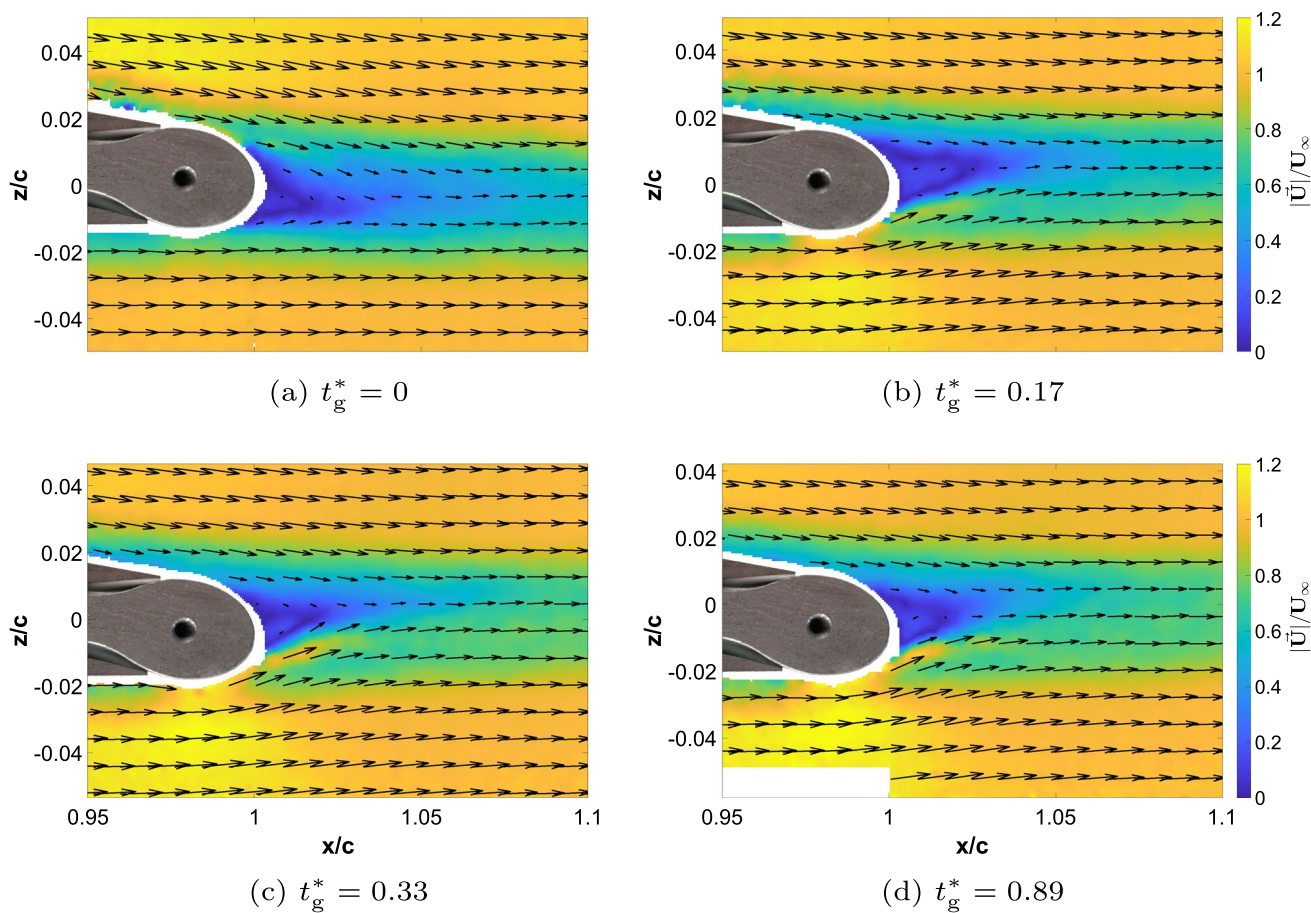


Fig. 18 Temporal evolution of flow field for impulsive switching from performance restoration to load alleviation

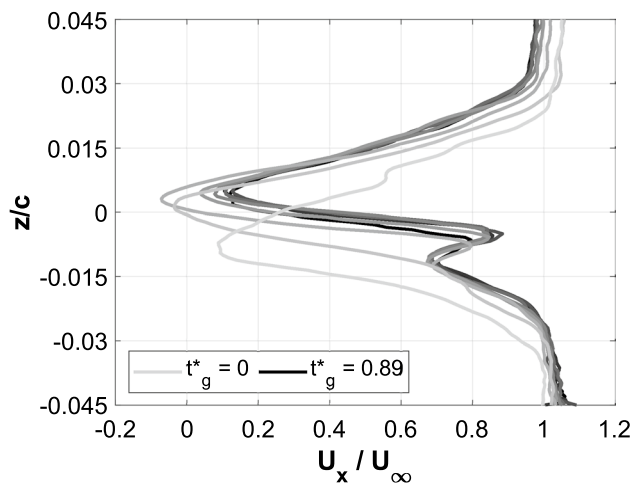


Fig. 19 Temporal evolution of wake velocity profiles  $U_x/U_\infty$  at  $x = 1.02c$  for impulsive switching from performance restoration to load alleviation

up, the main peak of the profile quickly jumps upwards and even features some slight reverse flow at the second observed point in time at  $\Delta t_g^* = 0.083$ . A secondary peak due to the lower jet starts to appear at  $\Delta t_g^* = 0.17$ , where the airfoil crosses through  $\Delta c_L \simeq 0$ . In the consecutive time steps the maximum velocity deficit slightly decreases and continues to slowly move further up, while the secondary velocity peak due to the lower blowing becomes more distinct. The results therefore show that right after the onset of the switching sequence already a large part of the wake reformation takes place, showing that the fast changes in wake structure due to the actuation outpace the global changes in lift.

The link between changes in local and global aerodynamics becomes more apparent when observing the surface pressure distribution on the airfoil, as shown in Fig. 20. Figure 20a shows the evolution on the upper side and Fig. 20b on the lower side of the airfoil. At  $t_g^* = 0$ , the upper jet effect is again still visible on the upper side of the trailing edge area in the form of a local suction peak. With the onset of the switching sequence, this suction peak reduces and a similar peak establishes on the lower side due to the lower

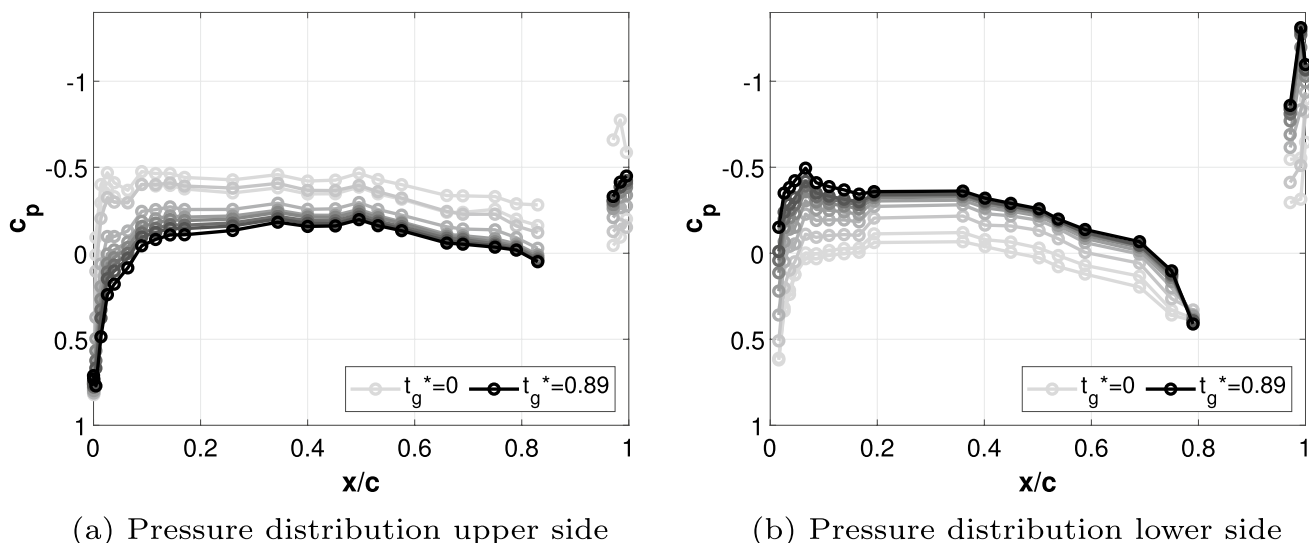


Fig. 20 Temporal evolution of pressure distribution for impulsive switching from performance restoration to load alleviation

jet establishment. Peak pressure values on the lower side of the order of  $c_p = -1.3$  are reached on the lower side compared to the achieved  $c_p = -0.77$  peak on the upper side, matching the different peak momentum coefficients of the two jets. On the main part of the wing, the  $c_p$  distribution moves towards higher pressures on the upper side and lower pressures on the lower side with advancing time. Similar to the steady measurements presented in Fig. 11, the two pressure curves cross each other as the lift switches over to negative values. As for the steady case, pressure change is found to be relatively uniform over the main part of the airfoil’s surface. It is found that the majority of the global surface pressure changes occurs over the initial four points in time presented here, followed by an asymptotic convergence to

the new state. A similar trend is found for the rear part of the airfoil, with the notable exception on the upper side of the Coandă surface, where a non-monotonous behavior is found that is potentially due to the onset and rapid suppression of vortex shedding around the zero lift crossing.

The flow fields are further analyzed with POD in Fig. 21. In particular, the impulsive switching from performance restoration to load alleviation and back to performance restoration is considered. The first mode in Fig. 21a contains 41% of the total kinetic energy and shows in absolute value a higher horizontal velocity than the freestream, both on the upper and lower side. It is noted that this amplitude is still modulated by the corresponding time coefficient of the POD, thus leading to reduced total amplitudes. The dominant

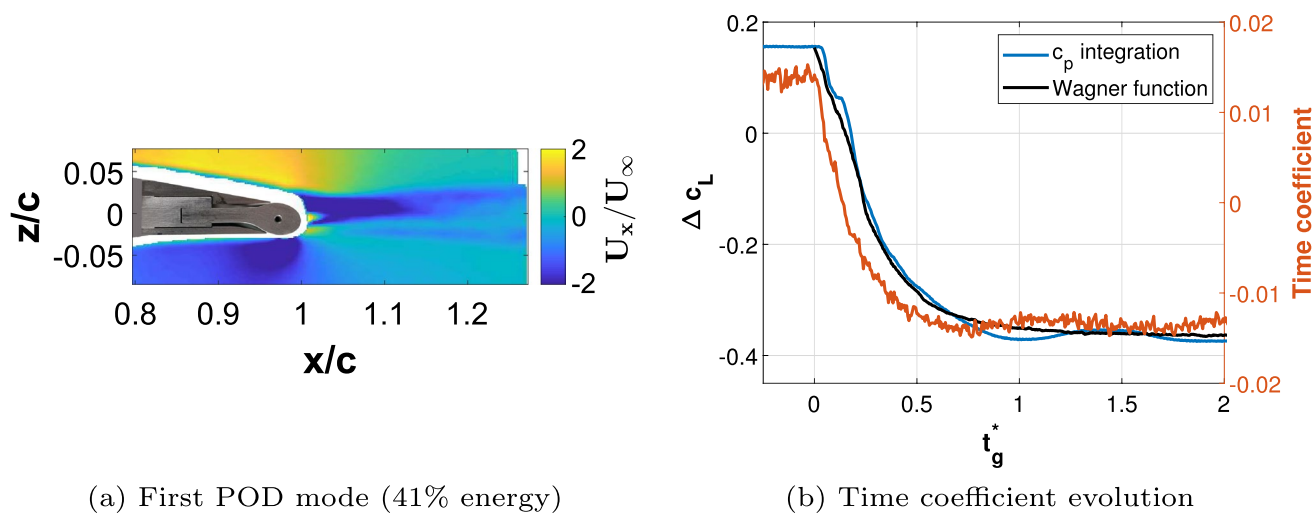


Fig. 21 First POD mode and its time coefficient for impulsive switching from performance restoration to load alleviation

mode features the entrainment of outer flow due to the jets, corresponding change in horizontal velocity above and below the airfoil, and persistence of the lower jet in the airfoil’s wake. The temporal evolution of the corresponding time coefficient is compared with the change in lift coefficient  $\Delta c_L$  in Fig. 21, exhibiting an overall similar trend. However, the time coefficient curve shows an earlier onset of the switching, with a time offset of about  $\Delta t_g^* = 0.12$  ( $\Delta t^* = 2.2$ ). Correspondingly, the steady value is reached already at  $t_g^* = 0.56$  for this POD mode, at the same time that the steady pressure level is reached in the plenum chamber and the main changes in the airfoil’s wake have materialized. As this POD mode was found to dominate the switching process of the flow field, this time delay can also be interpreted as the lag time of the response in surface pressure distribution and corresponding lift with respect to the flow field changes in the airfoil’s wake.

The impulsive jet actuation and corresponding aerodynamic response is further compared to the unsteady aerodynamics theory of Wagner. An impulsive change of an airfoil’s circulation, e.g. due to an impulsive change in angle of attack or impulsive surface jet activation, leads to the formation and detachment of a counter-rotating vortex of comparable circulation, which induces a downwash on the airfoil itself, resulting in reduced effective angle of attack and a consequent lift reduction compared to the steady state value. The vortex convects downstream with the freestream velocity, thereby diminishing the downwash effect over time according to the Biot-Savart law. The corresponding lift coefficient therefore does not follow the impulsive change in angle of attack or blowing directly, but exhibits an asymptotic convergence to the new steady value. The lift response

to impulsive blowing can then be described by the Wagner function  $\phi$  (Wagner 1924):

$$\Delta c_L = f(c_\mu) \cdot \phi(2 \cdot t^*) \tag{6}$$

Here  $f(c_\mu)$  is the amplitude of lift change  $\Delta c_L$  obtained by linear regression as a function of  $c_\mu$ . The Wagner function  $\phi$  is typically approximated, e.g. as proposed by Jones:  $\phi(2t^*) \approx 1 - 0.165e^{-0.0455 \cdot (2t^*)} - 0.335e^{-0.3 \cdot (2t^*)}$  (Jones 1938). The function equals 0.5 for  $t^* = 0$  and tends asymptotically to 1. For the given impulsive switching of  $c_\mu$  from performance restoration to load alleviation, the corresponding theoretical response of  $\Delta c_L$  after Wagner is added to Fig. 21b as a black curve. It is apparent that this approach shows overall very good agreement with the measured lift coefficient evolution and can therefore be used as a simple approximation of the lift response to impulsive Coandă jet activation.

Several other impulsive switching sequences were carried out to explore the dynamic behavior of the dual-slot circulation control airfoil for different blowing levels. This includes switching from maximum one-sided blowing to maximum blowing on the opposite side and various smaller steps in between, as shown in Fig. 22. The switching of the valves occurs at  $t_g^* = 0$ , from an initial to an alternate state (Fig. 22a) and back to the initial state (Fig. 22b). The combined measurement uncertainty of the changes in lift coefficient is added as narrow bands around the mean values, where the vertical extent of the bands corresponds to a 95% confidence interval in Fig. 22.

The load evolutions show high initial rates of change during both activation and deactivation, followed by asymptotic convergence to the respective quasi-steady lift coefficient. From the graphs, the switching time  $\Delta t_g^*$  is extracted as the

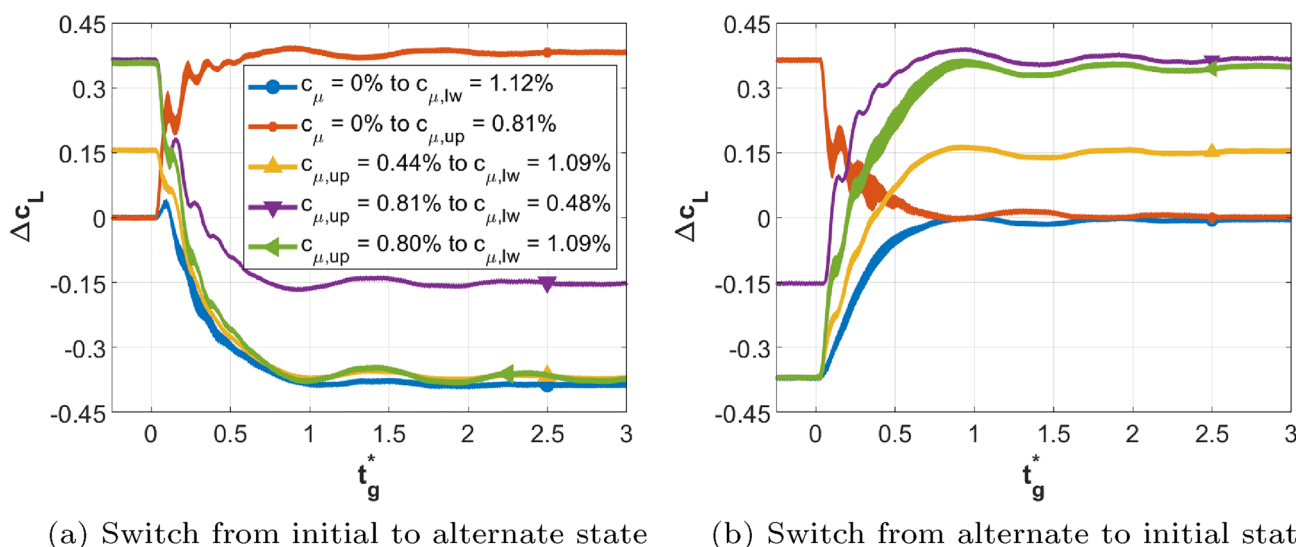


Fig. 22 Temporal evolution of  $\Delta c_L$  for several impulsive switching sequences

required time for the blowing to achieve 99% of the commanded lift change between the initial and alternate state. This time difference varies between a minimum of  $\Delta t_g^* = 0.80$  ( $\Delta t^* = 14.4$ ) for activation of full upper blowing from the unactuated airfoil and a maximum of  $\Delta t_g^* = 0.92$  ( $\Delta t^* = 16.6$ ) to switch from full upper to full lower blowing. Probably because of the increased system complexity, the lower slot blowing system features slightly longer onset times for both activation and deactivation. All tested conditions reach the targeted change before  $t_g^* = 1$ , i.e. before the fastest gust at the same freestream velocity could induce the maximum load change. The same two cases that encompass the full range of onset speeds also define the range of achievable load control authority of the system, between  $\Delta c_L = 0.36$  from unactuated airfoil to full upper and  $\Delta c_L = 0.73$  from full upper to full lower blowing. Some of the impulsive activation cases exhibit oscillations in the transient phase before reaching the new steady value. These oscillations are not related to any airfoil vibrations, which occur on a longer time-scale, but rather believed to be related to the vortex shedding at the onset of impulsive activation.

A comparison of the gust-induced loads at different Reynolds numbers  $Re$  and Mach numbers  $M_\infty$  is not straightforward. The freestream velocity but also the chord have a direct impact on when the peak load occurs on the wing but the ratio  $H/c$  also affects the load change because of unsteady aerodynamic effects. For comparison, the fastest gust defined in the certification documentation at ground level,  $M_\infty = 0.35$  and  $Re = 1.3 \cdot 10^7$  ( $c = 2.29$  m) generates a peak change in lift coefficient of  $\Delta c_L = 0.38$  at a slightly delayed time of  $\Delta t_g^* = 1.16$  ( $\Delta t^* = 4.54$ ), caused by unsteady aerodynamic effects. The highest gust load change ( $\Delta c_L = 0.68$ ) at ground level is reached for the longest gust with  $\Delta t_g^* = 10.2$  ( $\Delta t^* = 39.8$ ), (Asaro et al. 2021). Overall, the impulsive activation of the present actuation system appears to be fast enough to counteract even the shortest gusts encountered at ground level, but also features sufficient control authority to counteract the lift changes induced by the longest gusts.

For comparison, Geisbauer and Löser (2017) reported a similar impulsive activation of a mechanical spoiler at  $M_\infty = 0.2$  and  $Re = 2.7 \cdot 10^6$ . A lift change of  $\Delta c_L = -0.38$  was reached with a maximum spoiler deflection angle of  $\delta = 30^\circ$  at  $\Delta t_g^* = 1.91$  ( $\Delta t^* = 28.6$ ) with a deflection rate of  $120^\circ/s$ , which is already 30% higher than for the fast spoilers on conventional airplanes, according to Hueschen (2011). The frequently investigated conventional ailerons have even significantly smaller deflection rates than spoilers, on the order of  $35\text{--}40^\circ/s$  (McRuer and Council 1997). The deflection angles required to compensate the shortest gusts can therefore only be reached with a significant lead time through an advanced sensor system. Even if shorter gusts are

less relevant for the structural limit loads (Xu 2012), they affect structural fatigue and passenger comfort. In addition, a fast actuator response may also be required for longer gusts because of possible delays in the gust detection due to the employed sensors and controller.

## 4 Conclusion

The present work investigated the potential of a dual-slot Coandă-type flow control system for gust and maneuver load alleviation on a supercritical airfoil. The experimental tests were conducted in a low-speed wind tunnel at  $M_\infty \approx 0.14$  and a chord-based Reynolds number of  $Re \approx 1.5 \cdot 10^6$ . The flow actuator features an elliptical Coandă surface with slots on both upper and lower side with slot and lip heights of ca.  $0.08\%c$  or  $0.4$  mm.

The control authority of single slot blowing was quantified, with changes in lift coefficient reaching up to  $\Delta c_L \approx \pm 0.33$  relative to the unactuated airfoil, while achieving a high blowing efficiency, as characterized by lift-to-equivalent-drag ratio change of up to 100.

Simultaneous activation of both jets was found to reduce the equivalent drag compared to single jet blowing. Consequently, a small blowing rate ( $< 14\%$  of total blowing) added on the opposite side of the Coandă surface leads to increased lift-to-equivalent-drag ratio compared to single jet operation. Using small blowing rates for the lower and full blowing for the upper slot, the actuator's impact on airfoil pitching moment can be reduced compared to single jet operation with the same lift coefficient change.

Impulsive switching between different combinations of upper and lower slot blowing was investigated, exhibiting high lift control authority and fast actuation times. The flow field around the trailing edge of the airfoil reacts faster to the impulsive activation than the surface pressure and lift distributions. The Wagner function can be used to approximate the unsteady lift response due to the impulsive jet activation with sufficient accuracy. Blowing from one slot prior to activating the jet from the opposite slot does not adversely affect the actuation time of the system. The actuator shows high potential for counteracting typical gust-induced load changes with its high lift control authority and capability to reach the commanded load change faster than the shortest gust defined by certification documentation at ground level.

**Acknowledgements** We would like to acknowledge the funding by the Deutsche Forschungsgemeinschaft (DFG, German Research Foundation) under Germany's Excellence Strategy—EXC 2163/1-Sustainable and Energy Efficient Aviation—Project-ID 390881007.

**Author contributions** SA and AB: contributed to the study conception and design. Material preparation, data collection and analysis were performed by SA, in collaboration with Léon Lüer for the Particle Velocimetry Imaging part of the study. The first draft of the manuscript

was written by SA and all authors commented on previous versions of the manuscript. All authors read and approved the final manuscript.

**Funding** Open Access funding enabled and organized by Projekt DEAL. This study was funded by the Deutsche Forschungsgemeinschaft (DFG, German Research Foundation) under Germany's Excellence Strategy—EXC 2163/1- Sustainable and Energy Efficient Aviation—Project-ID 390881007.

**Data availability** The data presented in this work can be requested to the corresponding author.

## Declarations

**Conflict of interest** I declare that the authors have no competing interests as defined by Springer, or other interests that might be perceived to influence the results and/or discussion reported in this paper.

**Ethical approval** Not applicable.

**Open Access** This article is licensed under a Creative Commons Attribution 4.0 International License, which permits use, sharing, adaptation, distribution and reproduction in any medium or format, as long as you give appropriate credit to the original author(s) and the source, provide a link to the Creative Commons licence, and indicate if changes were made. The images or other third party material in this article are included in the article's Creative Commons licence, unless indicated otherwise in a credit line to the material. If material is not included in the article's Creative Commons licence and your intended use is not permitted by statutory regulation or exceeds the permitted use, you will need to obtain permission directly from the copyright holder. To view a copy of this licence, visit <http://creativecommons.org/licenses/by/4.0/>.

## References

- Abramson J (1975) Two-dimensional subsonic wind tunnel evaluation of a 20-percent-thick circulation control airfoil. Tech Rep, David W Taylor Naval Ship Research and Development Center, Bethesda, MD, USA
- Alexander MG, Anders SG, Johnson SK, et al (2005) Trailing edge blowing on a two-dimensional six-percent thick elliptical circulation control airfoil up to transonic conditions. American Society of Mechanical Engineers NASA/TM-2005-213545
- Asaro S, Khalil K, Bauknecht A (2021) Unsteady characterization of fluidic flow control devices for gust load alleviation. In: Dillmann A, Heller G, Krämer E, et al (eds) *New Results in Numerical and Experimental Fluid Mechanics XIII*, notes on numerical fluid mechanics and multidisciplinary design. Springer, p 152–163, [https://doi.org/10.1007/978-3-030-79561-0\\_15](https://doi.org/10.1007/978-3-030-79561-0_15)
- ASME (2006) Test uncertainty, ptc 19.1-2005. American Society of Mechanical Engineers
- Bauknecht A, Beyer Y, Schultz J, et al (2022) Novel concepts for active load alleviation. In: 2022 AIAA Scitech Forum. AIAA, San Diego, CA, USA
- Blaylock M, Chow R, Cooperman A et al (2014) Comparison of pneumatic jets and tabs for active aerodynamic load control. *Wind Energy* 17:1365–1384. <https://doi.org/10.1002/we.1638>
- Chambers JR (2005) Innovation in flight: research of the NASA Langley Research Center on revolutionary advanced concepts for aeronautics. National Aeronautics and Space Administration
- Darecki M, Edelstenne C, Enders T, et al (2011) Flightpath 2050 europe's vision for aviation. European Commission
- Düssler S, Siebert F, Bauknecht A (2022) Coanda-type flow actuation for load alleviation. *J Aircr*
- EASA (2020) Acceptable means of compliance for large aeroplanes cs-25. Amendment 24
- El Sayed Mohamed Y, Semaan R, Sattler S et al (2017) Wake characterization methods of a circulation control wing. *Exp Fluids* 58(10):1–17
- Englar RJ, Williams RM (1971) Design of a circulation control stern plane for submarine applications. Tech Rep, David W Taylor Naval Ship Research and Development Center Bethesda, MD
- Ewald B (1998) Wind tunnel wall correction. Tech Rep, AGARD-AG-336
- Geisbauer S, Löser T (2017) Towards the investigation of unsteady spoiler aerodynamics. In: 35th AIAA Applied Aerodynamics Conference, p 4229, Denver, CO, USA, June 5–9
- Hönlinger H, Zimmermann H, Sensburg O et al (1994) Structural aspects of active control technology. In: AGARD Conference Proceedings AGARD CP, AGARD, Turin, Italy, pp 18–18
- Hueschen RM (2011) Development of the transport class model (tcm) aircraft simulation from a sub-scale generic transport model (gtm) simulation. Tech Rep, NASA
- Jones RT (1938) Operational treatment of the nonuniform-lift theory in airplane dynamics. Tech Rep, NACA
- Jones GS (2005) Pneumatic flap performance for a 2d circulation control airfoil, stedy & pulsed. *Appl Circ Control Technol*, pp 191–244
- Khalil K, Asaro S, Bauknecht A (2021) Active flow control devices for wing load alleviation. *J Aircr* pp 1–17. <https://doi.org/10.2514/1.c036426>
- Li Y, Qin N (2020) Airfoil gust load alleviation by circulation control. *Aerospace Science and Technology* 98(105):622. <https://doi.org/10.1016/j.ast.2019.105622>
- McRuer DT, Council NR et al (1997) Aviation safety and pilot control: Understanding and preventing unfavorable pilot-vehicle interactions. National Academies Press
- Mickleboro HC (1948) Evaluation of a fixed spoiler as a gust alleviator. NACA Technical Note no. 1753
- Miklosovic D, Imber R, Britt-Crane M (2016) Measurements of mid-span flow interactions of a low-aspect-ratio circulation control wing. *J Aircr* 53:1969–1974. <https://doi.org/10.2514/1.c033852>
- Nishino T, Shariff K (2012) Effect of jet nozzle lip momentum loss on circulation control airfoil performance. *AIAA J* pp 551–558. <https://doi.org/10.2514/1.j051196>
- Radespiel R, Pfingsten KC, Jensch C (2009) Flow analysis of augmented high-lift systems. In: *Hermann Schlichting—100 Years*. Springer, pp 168–189
- Radespiel R, Burnazzi M, Casper M et al (2016) Active flow control for high lift with steady blowing. *Aeronaut J* 120:171–200. <https://doi.org/10.1017/aer.2015.7>
- Regan CD, Jutte CV (2012) Survey of applications of active control technology for gust alleviation and new challenges for lighter-weight aircraft. Tech Rep, NASA
- Semaan R (2020) The uncertainty of the experimentally-measured momentum coefficient. *Exp Fluids* 61:1–16. <https://doi.org/10.1007/s00348-020-03076-5>
- Sirovich L (1987) Turbulence and the dynamics of coherent structures, parts i, ii and iii. *Quart Appl Math* pp 561–590
- Spalart P, Shur M (1997) On the sensitization of turbulence models to rotation and curvature. *Aerosp Sci Technol* 1(5):297–302
- Swanson R, Rumsey C, Anders S (2005) Progress towards computational method for circulation control airfoils. In: 43rd AIAA Aerospace Sciences Meeting and Exhibit, p 89
- Wagner H (1924) Über die entstehung des dynamischen auftriebes von tragflügeln. Humboldt-Universität zu Berlin
- Warsop C, Crowther WJ (2018) Fluidic flow control effectors for flight control. *AIAA J* 56:3808–3824. <https://doi.org/10.2514/1.j056787>

- Welch P (1967) The use of fast fourier transform for the estimation of power spectra: a method based on time averaging over short, modified periodograms. *IEEE Trans Audio Electroacoust* 15(2):70–73
- Xu J (2012) Aircraft design with active load alleviation and natural laminar flow. PhD thesis, Stanford University

**Publisher's Note** Springer Nature remains neutral with regard to jurisdictional claims in published maps and institutional affiliations.